

Award Number: W81XWH-11-1-0248

TITLE: Echo-Planar Imaging Based J-Resolved Spectroscopic Imaging for Improved Metabolite Detection in Prostate Cancer

PRINCIPAL INVESTIGATOR: Michael Albert Thomas Ph.D.

CONTRACTING ORGANIZATION: University of California Los Angeles
Los Angeles, CA 90095

REPORT DATE: October 2012

TYPE OF REPORT: Annual

PREPARED FOR: U.S. Army Medical Research and Materiel Command
Fort Detrick, Maryland 21702-5012

DISTRIBUTION STATEMENT: Approved for Public Release;
Distribution Unlimited

The views, opinions and/or findings contained in this report are those of the author(s) and should not be construed as an official Department of the Army position, policy or decision unless so designated by other documentation.

REPORT DOCUMENTATION PAGE			<i>Form Approved</i> <i>OMB No. 0704-0188</i>		
Public reporting burden for this collection of information is estimated to average 1 hour per response, including the time for reviewing instructions, searching existing data sources, gathering and maintaining the data needed, and completing and reviewing this collection of information. Send comments regarding this burden estimate or any other aspect of this collection of information, including suggestions for reducing this burden to Department of Defense, Washington Headquarters Services, Directorate for Information Operations and Reports (0704-0188), 1215 Jefferson Davis Highway, Suite 1204, Arlington, VA 22202-4302. Respondents should be aware that notwithstanding any other provision of law, no person shall be subject to any penalty for failing to comply with a collection of information if it does not display a currently valid OMB control number. PLEASE DO NOT RETURN YOUR FORM TO THE ABOVE ADDRESS.					
1. REPORT DATE 25 October 2012		2. REPORT TYPE Annual		3. DATES COVERED 30 September 2011- 29 September	
4. TITLE AND SUBTITLE Echo-Planar Imaging Based J-Resolved Spectroscopic Imaging for Improved Metabolite Detection in Prostate Cancer			5a. CONTRACT NUMBER		
			5b. GRANT NUMBER W81XWH-11-1-0248		
			5c. PROGRAM ELEMENT NUMBER		
6. AUTHOR(S) Michael Albert Thomas Ph.D. E-Mail: athomas@mednet.ucla.edu			5d. PROJECT NUMBER		
			5e. TASK NUMBER		
			5f. WORK UNIT NUMBER		
7. PERFORMING ORGANIZATION NAME(S) AND ADDRESS(ES) University of California, Los Angeles Los Angeles CA, 90095			8. PERFORMING ORGANIZATION REPORT NUMBER		
9. SPONSORING / MONITORING AGENCY NAME(S) AND ADDRESS(ES) U.S. Army Medical Research and Materiel Command Fort Detrick, Maryland 21702-5012			10. SPONSOR/MONITOR'S ACRONYM(S)		
			11. SPONSOR/MONITOR'S REPORT NUMBER(S)		
12. DISTRIBUTION / AVAILABILITY STATEMENT Approved for Public Release; Distribution Unlimited					
13. SUPPLEMENTARY NOTES					
14. ABSTRACT . Purpose: 1) To implement an echo-planar imaging (EPI)-based 2D J-resolved spectroscopy on a 3T MRI/MRS scanner;2) To evaluate the multi-voxel 2D J-resolved echo-planar spectroscopic imaging (EP-JRESI) in malignant PCa patients, benign prostatic hyperplasia (BPH) patients and healthy prostates. 3) To develop and further optimize the ProFit algorithm to post-process the multi-dimensional MRS data from different prostate pathologies. Scope: A major outcome is expected to be on improved detection (specificity) in differentiating malignant from benign prostate cancer using a novel four-dimensional (4D) EP-JRESI. Improved spectroscopic imaging techniques will enable unambiguous detection of metabolites and the lipids in situ, which could potentially complement the existing diagnostic modalities commonly used in prostate cancer. Progress and Major Findings: The 4D EP-JRESI sequence was successfully implemented on a 3T MRI scanner using the Siemens IDEA pulse sequence compiler and multi-voxel 2D J-resolved spectra have been recorded using external as well as endorectal MRI coils. Endo-rectal 4D EP-JRESI data have been successfully recorded in 24 prostate cancer patients. Three peer-reviewed manuscripts have been published during the first year.					
15. SUBJECT TERMS- Digital Rectal Examination, prostate specific antigen, Four Dimensional (4D) Echo-Planar J-Resolved Spectroscopic Imaging (EP-JRESI); Citrate, Choline, Creatine, Spermine, 3Tesla MRI scanner, Endo-rectal MR coil, WET Water Suppression, prostate cancer (PCa), benign prostatic hyperplasia (BPH), prior-knowledge fitting					
16. SECURITY CLASSIFICATION OF:			17. LIMITATION OF ABSTRACT	18. NUMBER OF PAGES	19a. NAME OF RESPONSIBLE PERSON USAMRMC
a. REPORT U	b. ABSTRACT U	c. THIS PAGE U			
			UU	41	

Table of Contents

	<u>Page</u>
Introduction.....	4
Body.....	4
Key Research Accomplishments.....	9
Reportable Outcomes.....	10
Conclusion.....	10
References.....	11
Appendices.....	12

Introduction: Prostate cancer (PCa) is the most common cancer in men in several countries, with the American Cancer Society (ACS) estimating 241,740 new cases of PCa to be diagnosed and deaths of 28,170 men of PCa (1). Due to its prevalence in the male population as well as its unpredictable clinical course, early detection and diagnosis have become a priority for many health care professionals. Another method for staging prostate cancer is through imaging techniques including ultrasound, computed tomography (CT), and magnetic resonance imaging (MRI) with or without the help of dynamic contrast enhancement modeling (DCE-MRI), diffusion weighted imaging (DWI), and magnetic resonance spectroscopy (MRS) (2-5). MRS is a powerful tool for exploring the cellular chemistry of human tissues (3,5,6-11). There is a growing body of evidence that ¹H MRS may contribute to the clinical evaluation of prostate cancer and also for evaluating the metabolic alterations due to therapy. There have been no reports on combining two spectral dimensions with two-dimensional (2D) or three dimensional (3D) spatial encoding applicable to prostate cancer. Acceleration of magnetic resonance spectroscopic imaging (MRSI) has been demonstrated using echo-planar imaging techniques (12-13). Recently, Schulte et al. have successfully developed an algorithm called prior-knowledge fitting (ProFit) to quantify metabolite concentrations using the JPRESS spectra recorded using a Philips 3T MRI scanner (14). It was demonstrated that metabolite quantitation of JPRESS spectra with ProFit was accurate, robust and yielding generally consistent results, both *in vivo* and *in vitro*. Their results suggest that the number of quantifiable prostate metabolites can be increased from 3-4 with 1D PRESS/LC-Model to more than 10 with JPRESS/ProFit (15-16).

Body:

i) Proposed Task 1 (Months 1-6): To implement a multi-voxel based extension of the JPRESS sequence, in which two spectral encodings will be combined with two spatial encodings using the new Siemens VB17a platform. This four-dimensional (4D) data acquisition scheme will be accomplished utilizing the EPI approach that is commonly used for spatial encoding in MRI.

Accomplished during September 29, 2011-October 28 2012: The 4D echo-planar J-resolved spectroscopic imaging (EP-JRESI) sequence as shown in Fig.1 was successfully compiled using the Siemens VB17a compiler. The volume of interest (VOI) was localized using three selective radio-frequency (RF) pulses similar to the PRESS sequence that is routinely used by MR researchers around the world. There were B₀ crusher gradient pulses around the two refocusing 180⁰ (π) RF pulses. The EPI read-out

enabled readout of 512 maximum t_2 spectral points and $16k_x$ spatial points. Remaining spectral and spatial encodings were accomplished using incremented Δt_1 and k_y . Total echo time ($TE = TE_1 + TE_2$) was 30 ms. The 4D raw data was typically $512t_2 * 64 - 100t_1 * 16k_x * 16k_y$. Since the 4D EP-JRESI sequence is a home-built sequence, there is no manufacturer supplied extraction program to post-process the acquired data. Hence, our group had to develop extraction codes using the MATLAB library.

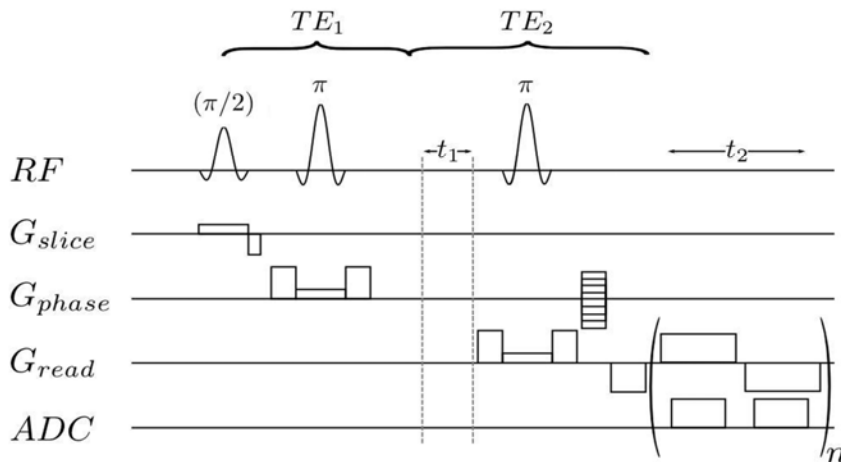


Figure.1. The 4D EPJRESI sequence showing two spatial encodings (k_x, k_y) and two spectral encodings (t_2, t_1). Inherent acceleration of k_x and t_2 is enabled here by the echo-planar imaging (EPI)-based read-out.

ii) **Proposed Task 2:** To evaluate the EPI-based JPRESS using a prostate phantom containing several metabolites which have been reported in prostate tissues, and to optimize the EP-JRESI sequence and other acquisition parameters using the phantom (Months 6-12).

Accomplished during September 29, 2011-October 28 2012: The sequence was tested using a prostate phantom containing 10 different metabolites at physiological concentrations (pH set to 7.2). A 500 ml prostate phantom was prepared containing the following metabolites at physiological concentrations as reported in healthy human prostate (15-16): Citrate (Cit, 50mM), Creatine (Cr, 5mM), Choline (Cho, 1mM), Spermine (Spm, 6mM), myo-inositol (mi, 10mM), Phosphocholine (PCh, 2mM), Taurine (Tau, 3mM), Glutamate (Glu, 4mM), Glutamine (Gln, 2.5mM) and Scyllo-Inositol (sl, 0.8mM). Shown in Fig.2A is an axial MRI slice image showing the multi-voxel grids of MRSI with the yellow boundary of the field of view (FOV), and the white box representing the volume of interest (VOI) localized by the PRESS sequence which is an integral part of the EP-JRESI sequence. The following parameters were used for acquiring the fully sampled EP-JRESI data: $TR/TE = 1500/30ms$, 16 phase encodes (k_y), 32 read-out points

(k_x) with oversampling, 512 \pm read-out trains resulting in 512 pairs of complex spectral points in the 2nd spectral dimension (t_2), 100 t_1 increments for the indirect spectral dimension and one average per encoding. A total duration of 40 minutes was necessary to acquire this water-suppressed EP-JRESI data. A non-water-suppressed EP-JRESI data using 4 averages with only one t_1 increment was used for eddy current and phase correction of the suppressed data (14). After apodization and Fourier transformation of this 4D data, the reconstructed multi-voxel 2D J-resolved spectra (shown in C) were overlaid on top of the 16x16 spatial grids. An extracted 2D J-resolved spectrum (3ml) around the center of the VOI is shown in Fig. 2B.

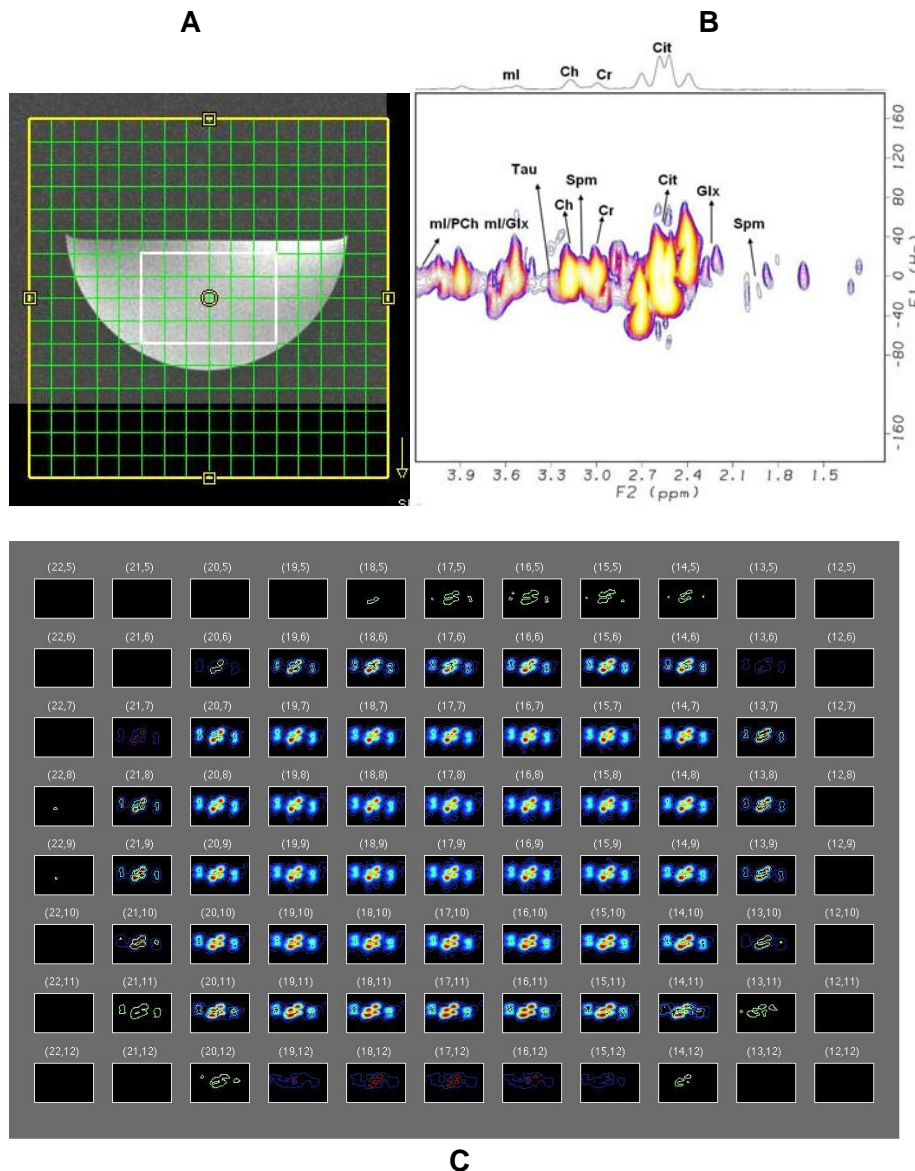


Figure 2.A. An MRI axial slice image of the prostate phantom showing the VOI localization (white box) and field of view (FOV) for spatial encoding (yellow grids). **B.**

Extracted 3ml 2D J-resolved spectrum from the center of the phantom. **C.** Multi-voxel display of Cit recordable within the white box boundary; the peaks outside the VOI are due to Gibb's ringing or bleed.

As mentioned before, Fig.2 demonstrates the successful implementation of the 4D EP-JRESI sequence on the 3T MRI scanner. Significant programming efforts were necessary for accomplishing this on both acquisition and post-processing fronts.

iii) Proposed Task 3: To record the 4D EP-JRESI spectra in the peripheral, central and transition zones of malignant, benign and healthy prostates. (**Months 6-12**).

Accomplished during September 29, 2011-October 28 2012: A 32 yo healthy human subject was investigated on the 3T MRI scanner using the quadrature body coil “transmit” and external body matrix “receive” coil assembly. The following parameters were used to acquire the EP-JRESI data: TR/TE=1.5s/30ms, 2 averages, 512 t_2 , oversampled 32k_x, 64 increments along the indirect spectral (t_1) and 16 spatial k_y dimensions. In Fig. 3A, an axial MRI of the abdomen is shown displaying the VOI covering the prostate localized by the PRESS sequence and the EP-JRESI grids. The multi-voxel display of a selected region is shown in Fig. 3B. The 2D J-resolved spectrum (2ml) extracted from the location (*) is shown in Fig. 3C. The 2D diagonal and cross peaks of Cit and other metabolites are visible. As shown below, the endorectal “receive” coil is expected to facilitate at least one order of magnitude higher sensitivity than that of the body matrix assembly used here.

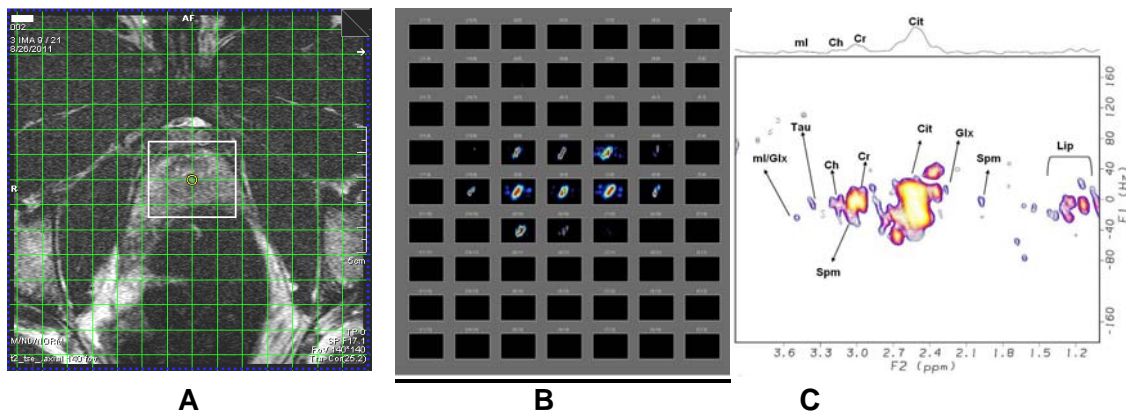


Figure 3. A. An axial MRI slice of the 32y.o. healthy male subject showing the VOI and MRSI grids. **B.** Expanded multi-voxel 2D spectra showing the Cit multi-voxels. **C.** The 2D J-resolved spectrum extracted from a 2ml voxel of the peripheral zone.

Using the endorectal "receive" coil, another 4D EP-JRESI data acquired in a 61 year old PCa patient having PSA of 9.1 and two malignant lesions (GS3+4 in the right

base and GS4+3 in the right mid regions) and extracted spectra from 2 different locations (1ml) are shown in Figure 4. The extracted two spectra from the malignant masses in the right mid (GS4+3) (ii) and right base (iii) regions, and iv) healthy peripheral zone.

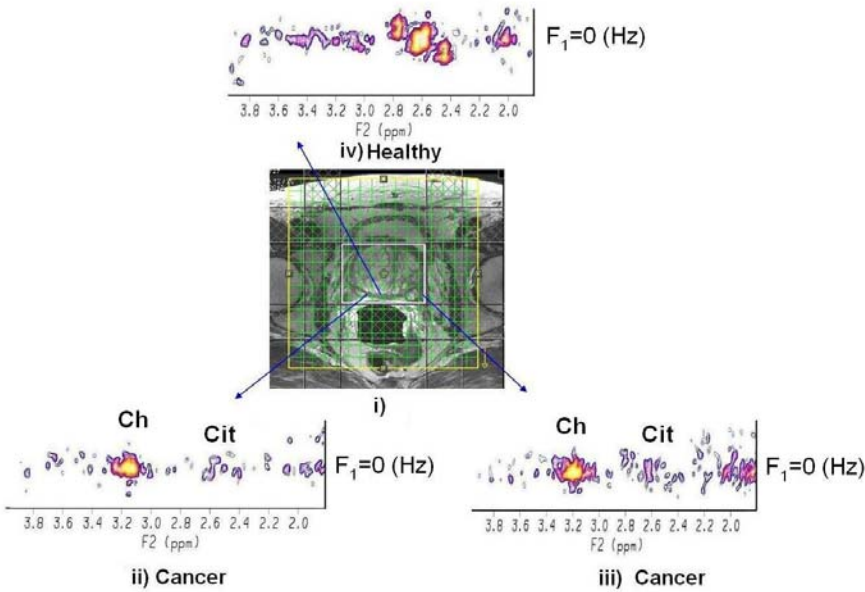


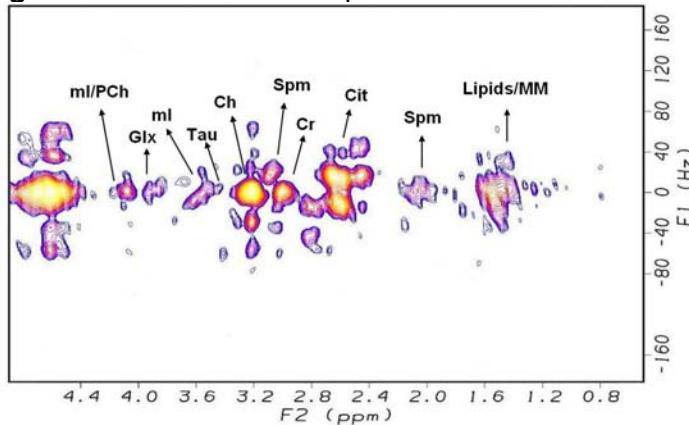
Figure 4. i) An axial T₂W MRI slice showing the multi-voxel EP-JRESS grids; extracted 2D JPRESS spectra of malignant voxels (ii) and (iii), and the healthy voxel in the peripheral zone (iv).

iv) Proposed Task 4: To develop, evaluate and optimize the prior-knowledge basis set spectra using the GAMMA-simulation and prostate phantom solutions as prior knowledge for the multi-voxel based JPRESS spectra recorded using the 3T MRI scanner (Months 6-12).

Accomplished during September 29, 2011-October 28 2012:

Shown in Fig.5 is a 2D J-Resolved spectrum recorded in a 27 y.o. healthy male. Presence of several metabolites is clearly marked here. More than 10 basis-sets were constructed for the prior-knowledge fitting developed using the GAMMA library (17).

Figure 5. A 2D J-resolved spectrum recorded in a healthy male prostate.



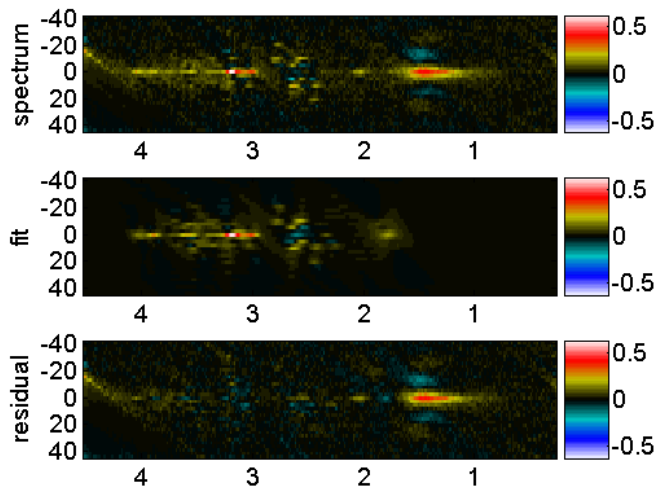


Figure 6. Prior-knowledge J-resolved spectra for the prostate metabolites: Experimental (top), fitted using ProFit algorithm (middle) and residual (bottom).

Shown in Fig.6 are 2D plots showing ProFit quantitation using MATLAB codes. Using the spectral data recorded in the peripheral zone of the 27y.o. healthy volunteer, following ratios were quantified (/Cr): PCh: 0.09, Cit: 7.36, Spm: 8.55, Glycerlphosphocholine (GPC): 0.483, Cho: 0.01, ml:3.79, sl:0.012, Tau:1.47, Gln: 0.03, Glu:1.52. These preliminary results show the feasibility of detecting more metabolites in the 4D EP-JRESI spectrum than the conventional MRSI showing 3-4 metabolites only.

Key Research Accomplishments

- Implementation of the 4D EP-JRESI sequence on the Siemens 3T and 1.5T MRI scanners after the C++ compilation of the sequence using the Siemens IDEA VB17a compiler.
- Prior-knowledge basissets have been developed for prostate metabolites such as Cit, choline groups containing glycerylphosphocholine, phosphocholine, Cr, Spm, ml, Glu, Gln, sl, phosphoethanolamine and lactate using a GAMMA C++ library. Prostate metabolite quantitation has been tested using the ProFit algorithm.
- Evaluation of the 4D EP-JRESI sequence in 24 malignant and benign prostate cancer patients.
- Recent progress has been made on further acceleration of the 4D EP-JRESI sequence using non-uniform undersampling (NUS) and compressed sensing (CS) reconstruction. This will enable shortening the endorectal spectral acquisition and reducing the patient inconvenience during the scan.
- Using the preliminary results obtained using this IDEA grant, an R01 application entitled "EchoPlanar J-resolved Prostate Cancer Metabolite Imaging Using Compressed Sensing" was submitted to the National Institute of health (NIH) in July2012/October 2011. In the October 2012 review, my revised application received a non-fundable 32nd percentile score only as the National Cancer Institute's funding is currently below 10th percentile only.

Reportable Outcomes:

A. Peer-reviewed Publications:

1. Nagarajan R, Margolis D, Raman S, et al. MR Spectroscopic Imaging and Diffusion-Weighted Imaging of Prostate Cancer With Gleason Scores. *J Magn Reson Imaging* 2012;36:697-703 [PMID: 22581787].
2. Nagarajan R, Margolis D, Raman S, et al. Correlation of Gleason Scores with Diffusion-Weighted Imaging Findings of Prostate Cancer. *Advances in Urology* 2012; 2012:374805. Epub 2011 Dec 15 [PMID: 22216026].
3. McClure TD, Margolis DJ, Reiter RE, et al. Use of MR imaging to determine preservation of the neurovascular bundles at robotic-assisted laparoscopic prostatectomy. *Radiology*. 2012 Mar;262(3):874-83. Epub 2012 Jan 24 [PMID: 22274837].
4. Furuyama J, Wilson NE, Burns BL, et al. Application of Compressed Sensing to Multidimensional MR Spectroscopic Imaging in Human Prostate. *Magn Reson Med* 2012;67:1499-1505 [PMID: 22505247].

B. Presentations: During this year, the first abstract entitled "Novel Multi-dimensional Magnetic Resonance Spectroscopic Imaging: Implementation and Pilot Validation in Prostate and Breast Cancer in vivo" was submitted and presented as an invited talk at the 17th International Biophysics Congress (IUPAB) conference in Beijing, China (Oct.30-Nov.3, 2011). The 2nd abstract summarizing the implementation of the 4D EP-JRESI sequence and evaluation of it in healthy males was presented at the 2011 Radiological Society of Northern America (RSNA) meeting (Nov.-Dec.2011) in Chicago, IL. 2012. Third abstract entitled "Accelerated Multi-Voxel Two-Dimensional In Vivo Spectroscopy Using Compressed Sensing" was presented at the 53rd Experimental NMR Conference (ENC) meeting in Miami, Florida (April 15-20, 2012). Fourth Abstract entitled "Accelerating Echo-Planar J-Resolved Spectroscopy of the Prostate using Compressed Sensing in a Clinical Setting" was presented at the 20th International Society of Magnetic Resonance in Medicine (ISMRM) meeting in Melbourne, Australia (May 5-11, 2012).

C. Books: None on Prostate Cancer Research based.

Conclusions: First few months of the 1st year were spent in getting the approval from the HSRRB and UCLA IRB offices. The 4D EP-JRESI scanning protocol was successfully implemented on the 3T MRI scanner. After optimizing the protocol using phantom solutions containing metabolites and corn oil, the protocol has been successfully tested in healthy males, and malignant and BPH patients. We will continue to recruit 20 malignant and 5 benign prostate cancer patients, and 5 healthy males during the next year.

References

- 1) Dall'era MA, Cooperberg MR, Chan JM, *et al.* Active surveillance for early-stage prostate cancer: review. *Cancer*. 2008 Apr 15;112(8):1650-9. **PMID: 18306379**
- 2) McNeal JE. Normal histology of the prostate. *Am J Surg Pathol* 1988;12:619-633. **PMID: 2456702**
- 3) Weinreb JC, Blume JD, Coakley FV, *et al.* Prostate cancer: sextant localization at MR imaging and MR spectroscopic imaging before prostatectomy--results of ACRIN prospective multi-institutional clinicopathologic study. *Radiology*. 2009 Apr;251(1):122-33. **PMID: 19332850**
- 4) Jacobs MA, Ouwerkerk R, Petrowski K and Macura KJ. Diffusion-weighted imaging with apparent diffusion coefficient mapping and spectroscopy in prostate cancer. *Top Magn Reson Imaging*. 2008;19:261-72 **PMID:19512848**
- 5) Scheenen TW, Heijmink SW, Roell SA, *et al.* Three-dimensional proton MR Spectroscopy of human prostate at 3T without endorectal coil: feasibility. *Radiology* 2007;245:507-16. **PMID: 17848681**
- 6) Thomas MA, Narayan P, Kurhanewicz J, Jajodia P, Weiner MW. 1H MR spectroscopy of normal and malignant human prostates in vivo. *J Magn Reson* 1990; 87:610-619. **PMID:N/A**
- 7) Thomas MA, Narayan P, Kurhanewicz J, *et al.* Detection of phosphorus metabolites in human prostates with a transrectal ³¹P NMR probe. *J Magn Reson* 1992; 99: 377-386. **PMID: N/A**
- 8) Narayan P, Kurhanewicz J. Magnetic Resonance spectroscopy in prostate disease: diagnostic possibilities and future developments. *Prostate* 1992; Suppl 4: 43-50. **PMID: 1374177**
- 9) van der Graaf M, Schipper RG, Oosterhof GO, J.A. Schalken, AA. Proton MR spectroscopy of prostatic tissue focused on the detection of spermine, a possible biomarker of malignant behavior in prostate cancer. *MAGMA* 2000; 10(3):153-9. **PMID: 10873205**
- 10) Jordan KW and Cheng LL. NMR-based metabolomics approach to target biomarkers for human prostate cancer. *Expert Rev Proteomics* 2007;4:389-400. **PMID: 17552923**
- 11) Kurhanewicz J, Swanson MG, Nelson SJ, and Vigneron DB. Combined magnetic resonance imaging and spectroscopic imaging approach to molecular imaging of prostate cancer. *J Magn Reson Imaging* 2002;16(4):451-463. **PMID: 12353259**
- 12) Mansfield P. Spatial mapping of the chemical shift in NMR. *Magn Reson Med* 1984; 1: 370 - 386. **PMID:6571566**
- 13) Posse S, Otazo R, Caprihan A, *et al.* Proton echo-planar spectroscopic imaging of J-coupled resonances in human brain at 3 and 4 Tesla. *Magn Reson Med* 2007; 58(2): 236-44. **PMID: 17610279**
- 14) Schulte RF and Boesiger P. ProFit: two-dimensional prior-knowledge fitting of J-resolved spectra. *NMR Biomed* 2006;19:255-263. **PMID: 16541464**
- 15) Lange T, Schulte RF and Boesiger P. Quantitative J-resolved prostate spectroscopy using two-dimensional prior-knowledge fitting. *Magn Reson Med* 2008;59:966-972. **PMID: 18429013**
- 16) Thomas MA, Lange T, Velan SS, *et al.* Two-dimensional MR Spectroscopy of healthy and cancerous prostates in vivo. *Magn Reson Mater Phy (MAGMA)* 2008;21(6):443-58. **PMID: 18633659**
- 17) Smith SA, Levante TO, Meier BH and Ernst RR. Computer Simulations in Magnetic Resonance. An object oriented programming approach. *J Magn Reson* 1994; A106: 75-105. **PMID: N/A**

Appendix:

1. Nagarajan R, Margolis D, Raman S, et al. MR Spectroscopic Imaging and Diffusion-Weighted Imaging of Prostate Cancer With Gleason Scores. *J Magn Reson Imaging* 2012;36:697-703.
2. Nagarajan R, Margolis D, Raman S, et al. Correlation of Gleason Scores with Diffusion-Weighted Imaging Findings of Prostate Cancer. *Advances in Urology* 2012; 2012:374805. Epub 2011 Dec 15.
3. McClure TD, Margolis DJ, Reiter RE, et al. Use of MR imaging to determine preservation of the neurovascular bundles at robotic-assisted laparoscopic prostatectomy. *Radiology*. 2012 Mar;262(3):874-83. Epub 2012 Jan 24.
4. Furuyama J, Wilson NE, Burns BL, et al. Application of Compressed Sensing to Multidimensional MR Spectroscopic Imaging in Human Prostate. *Magn Reson Med* 2012;67:1499-1505.

Original Research

MR Spectroscopic Imaging and Diffusion-Weighted Imaging of Prostate Cancer With Gleason Scores

Rajakumar Nagarajan, PhD,¹ Daniel Margolis, MD,¹ Steven Raman, MD,¹ Manoj K. Sarma, PhD,¹ Ke Sheng, PhD,² Christopher R. King, MD, PhD,² Gaurav Verma, PhD,¹ James Sayre, PhD,¹ Robert E. Reiter, MD,³ and M. Albert Thomas, PhD^{1*}

Purpose: To investigate functional changes in prostate cancer patients with three pathologically proven different Gleason scores (GS) (3+3, 3+4, and 4+3) using magnetic resonance spectroscopic imaging (MRSI) and diffusion-weighted imaging (DWI).

Materials and Methods: In this study MRSI and DWI data were acquired in 41 prostate cancer patients using a 1.5T MRI scanner with a body matrix combined with an endorectal coil. The metabolite ratios of (Cho+Cr)/Cit were calculated from the peak integrals of total choline (Cho), creatine (Cr), and citrate (Cit) in MRSI. Apparent diffusion coefficient (ADC) values were derived from DWI for three groups of Gleason scores. The sensitivity and specificity of MRSI and DWI in patients were calculated using receiver operating characteristic curve (ROC) analysis.

Results: The mean and standard deviation of (Cho+Cr)/Cit ratios of GS 3+3, GS 3+4, and GS 4+3 were: 0.44 ± 0.02 , 0.56 ± 0.06 , and 0.88 ± 0.11 , respectively. For the DWI, the mean and standard deviation of ADC values in GS 3+3, GS 3+4, and GS 4+3 were: 1.13 ± 0.11 , 0.97 ± 0.10 , and 0.83 ± 0.08 mm²/sec, respectively. Statistical significances were observed between the GS and metabolite ratio as well as ADC values and GS.

Conclusion: Combined MRSI and DWI helps identify the presence and the proportion of aggressive cancer (ie, Gleason grade 4) that might not be apparent on biopsy sampling. This information can guide subsequent rebiopsy management, especially for active surveillance programs.

Key Words: MR spectroscopy; prostate cancer; diffusion weighted imaging; apparent diffusion coefficient; Gleason scores

J. Magn. Reson. Imaging 2012;36:697-703.

© 2012 Wiley Periodicals, Inc.

PROSTATE CANCER (PCa) is the most common cancer in men and is the second leading cause of cancer death in American men, behind only lung cancer. Prostate cancer affects over 200,000 men each year and causes 27,000 deaths annually in the United States (1). Early PCa detection is the key to successful cancer treatment. To date, the suspicion of PCa is mainly based on elevated serum prostate-specific antigen (PSA) or abnormal digital rectal examination (DRE) of the prostate, both with well-known limitations (2,3). Systematic but untargeted transrectal ultrasound (TRUS)-guided biopsy is the standard method for histological diagnosis of PCa (4). However, untargeted systematic biopsies have several disadvantages: they miss cancer in up to 35% of cases (4), multiple foci of cancer are present in more than 85% of cases of PCa (5), and complications may occur because of unnecessary biopsies. Therefore, a noninvasive diagnostic method would clearly be beneficial.

The pathologic grade, or aggressiveness, of PCa is given by the Gleason score (6). The Gleason grading system consists of two digits, the primary and secondary pattern in the tumor. Gleason patterns are numbered in increasing order of cellular disorder and loss of normal glandular architecture from 1 to 5, with 1 being the least aggressive and 5 the most aggressive. A Gleason score (GS) of 6 or less is considered low grade (ie, all pattern 3 or lower); 7 (ie, 3+4 or 4+3), intermediate grade; and 8 through 10 (some component of pattern 4 or 5), high grade. A tumor with a low GS typically grows slowly enough that it may not pose a significant threat to the patient in his lifetime.

Increased choline (Cho) and reduced citrate (Cit) have been demonstrated by 3D magnetic resonance spectroscopic imaging (MRSI) of PCa. Since creatine (Cr) is not resolvable from Cho in the prostate at 1.5T, combined Cho+Cr is used. The decrease in Cit in PCa

¹Department of Radiological Sciences, David Geffen School of Medicine, University of California, Los Angeles, California, USA.

²Department of Radiation Oncology, David Geffen School of Medicine, University of California, Los Angeles, California, USA.

³Department of Urology, David Geffen School of Medicine, University of California, Los Angeles, California, USA.

Contract grant sponsor: IDEA Grant from the Department of Defense (DOD) prostate cancer research program; Contract grant number: W81XWH-11-1-0248.

*Address reprint requests to: M.A.T., Radiological Sciences, David Geffen School of Medicine at UCLA, 10833 Le Conte Ave., Los Angeles, CA 90095-1721. E-mail: athomas@mednet.ucla.edu

Received October 24, 2011; Accepted March 14, 2012.

DOI 10.1002/jmri.23676

View this article online at wileyonlinelibrary.com.

is due to both changes in cellular function (eg, increased metabolism and consumption of tricarboxylic acid cycle metabolites) and in the organization of the tissue, with loss of its characteristic ductal morphology (7,8). The elevation of the Cho peak in PCa is associated with changes in cell membrane synthesis and degradation that occur with the evolution of human cancer (9,10). MR spectroscopy offers improved sensitivity and specificity for PCa detection (11–13). There are several reports during the last decade demonstrating the application of diffusion-weighted imaging (DWI) in PCa and these findings look promising (14–17). It is straightforward to implement, with shorter image acquisition times and the availability of quantitative data using apparent diffusion coefficient (ADC) values.

Magnetic resonance methods have shown promising results in the diagnosis of PCa (18,19). T₂-weighted (T2W) MRI can depict prostate zonal anatomy (20,21). MRSI provides information about relative concentrations of cellular metabolites in the prostate (22,23). DWI characterizes the tissue structure at the microscopic level (24).

The purpose of the study was to assess the effectiveness of the combined 3D MRSI with DWI investigation of PCa patients with a progressively increasing proportion of aggressive cancer (GS 3+3, GS 3+4, and GS 4+3).

MATERIALS AND METHODS

Patients

Between February 2007 and June 2008, 41 patients (GS 3+3 [*n* = 12], GS 3+4 [*n* = 20] and GS 4+3 [*n* = 9]) who underwent radical prostatectomy were selected for the endorectal MR study. At least 6 weeks were recommended between the biopsy and MRI due to the interference of postbiopsy hemorrhage with the images. The Investigational Review Board approved our retrospective study and waived the informed consent requirement. The ages of the patients ranged from 47 to 75 years, or, by GS category, GS: 3 + 3 (mean ± standard deviation [SD], 60.1 ± 6.7 years), 3 + 4 (mean ± SD, 58.1 ± 4.2 years), and 4 + 3 (mean ± SD, 60.3 ± 3.9 years). The mean PSA values for the patients with GS 3+3, GS 3+4, and GS 4+3 were 5.1 ng/ml, 6.7 ng/ml, and 7.3 ng/ml, respectively.

MRI/DWI

The MRI/MRSI data were acquired on a 1.5T Avanto-Tim MRI/MRS scanner with high-performance gradients (Siemens Medical Solutions, Erlangen, Germany). A combined body matrix phased-array coil assembly and an endorectal coil were used in the “receive” mode while a quadrature body coil was used for “transmit.” After acquiring the T₁-weighted imaging (repetition time / echo time [TR/TE] = 540/11 msec), thin-section high-spatial-resolution transverse, sagittal, and coronal T₂-weighted fast spin-echo images of the prostate and seminal vesicles were obtained with the following parameters: 3800/101 msec (effective);

echo train length, 32; section thickness, 3 mm; intersection gap, 0 mm; field of view (FOV), 14 cm; matrix, 205 × 256.

Axial DWI images were recorded using the single-shot echo planar imaging technique using the following imaging parameters: TR/TE 2000/83 msec, 27 cm FOV, 4-mm slice thickness, 0 mm intersection gap, 3 averages. Isotropic DWIs were obtained using diffusion gradients with three b-values (0, 50, and 400 sec/mm²) along three directions of motion-probing gradients. Due to the use of lower field, low b-values were chosen for the DWI. Higher b-values are associated with an increased background noise. Also, this protocol was based on the earlier protocol developed for general body imaging. The orientation and location of these images were prescribed identically to the transverse T₂-weighted prostate images.

MRSI

MRSI was performed in all patients with water- and fat-suppressed acquisition. The 3D MRSI parameters were as follows: TR/TE = 700/120 msec; 6 averages; spectral width, 1300 Hz; number of complex points, 512; FOV, 80 × 80 × 80 mm³; 12 × 12 × 12 phase-encoding steps to accomplish spatial encoding along three dimensions. A point-resolved spectroscopy sequence (PRESS) was used to acquire the proton (¹H) MR spectra from a volume of interest of 55 × 40 × 40 mm³. The MRSI voxel volume was 0.3 cm³. Outer volume lipid suppression was achieved using eight 3-cm slab saturation pulses around the volume of interest. Water and fat resonances were suppressed using two 12.6-msec dual-frequency selective MEGA pulses (25) with B₀ crusher gradients. The total acquisition time was ≈14 minutes including the voxel prescription, shimming, and prescan optimization. The full width at half maximum (FWHM) of the water peak was ≈12 Hz.

Data Analysis: MRSI and DWI

The MRSI postprocessing software on the MR scanner provided by the manufacturer was used to evaluate the (Cho+Cr)/Cit ratios. Postprocessing of the time domain data extracted from MRSI multiple voxels consisted of zero filling from 512 to 1024 data points, multiplication by a Hamming filter, Fourier transformation, and phase and baseline correction. We obtained the integral values by fitting Gaussian line shape functions to the resulting absorption spectra. For further analysis, ratios of integrals (Cho+Cr)/Cit were used. The MRSI was overlaid onto a T2W image, and Digital Imaging and Communications in Medicine (DICOM) position information was used to find the closest match. In patients with histologically proven prostate carcinoma, the voxels covering the tumorous lesions from the peripheral zone (PZ) were selected and indicated as tumor voxels. Voxels were considered sufficient for analysis if one of the metabolites had a signal-to-noise ratio (SNR) of at least 4:1.

In the DWI, the mean ADCs and SD of peripheral zone cancer was calculated from regions of interest

Table 1
Statistically Significant Mean ADC Value, MR Spectroscopic Ratio, and Tumor Volume of Three Gleason Scores

Gleason scores	(Cho+Cr)/Cit ratio mean (range)	Mean ADC (range) (mm ² /sec)	Tumor volume (cc)
3+3	0.44 (0.34–0.49)	1.13 (0.91–1.33)	1.54 (0.5–3.5)
3+4	0.56 (0.46–0.73)	0.97 (0.70–1.11)	1.96 (0.5–4.6)
4+3	0.88 (0.75–1.05)	0.83 (0.74–1.01)	2.77 (0.5–5)

(ROIs) defined by the histological findings of the radical prostatectomy specimens and compared to the T₂-weighted imaging. The MRI sections and histological slices were matched based on the level sextant locations, anterior/posterior and central/peripheral. Each sextant was biopsied twice for 12 to 14 cores. The ROI of the same size and location from each method were drawn manually on the ADC maps and DWI by a single reader. When the ROIs were drawn, care was taken to exclude both the neurovascular bundle and the urethra to reduce any error in ADC calculations. If a tumor was located in several imaging slices of ADC maps, ADC values were measured on each image of the ADC maps and the average was calculated. The histology was reviewed by an experienced dedicated genitourinary pathologist.

Statistical Analysis

A one-way analysis of variance (ANOVA) was performed to assess the statistical differences between MRSI values and Gleason scores and between ADC values and Gleason scores. Spearman's rank correlation coefficients were used to characterize the association of the ADC values and MRSI ratios for tumors with the Gleason score and pathologically determined tumor volume.

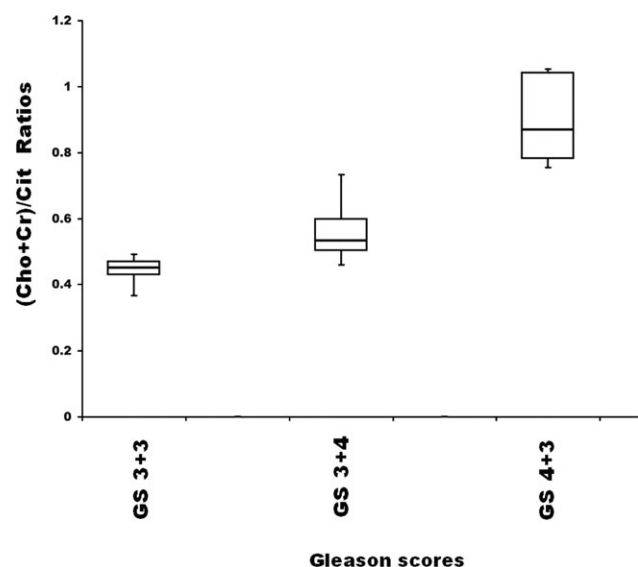


Figure 1. Box-and-whisker plot shows the MR spectroscopic ratios of three Gleason scores (GS 3+3, GS 3+4, and GS 4+3).

Receiver operating characteristic (ROC) curve analyses based on logistic regression models were performed in order to identify the optimal cutoff value for ADC and metabolite ratios for prediction purposes of three different Gleason scores. The area under the curve (AUC), interpreted as the average value of sensitivity for all possible values of specificity, was taken as a criterion for the success of the ROC analysis. An area of 0.50 implies that the variable adds no information, whereas an area of 1 implies perfect accuracy. Sensitivity, specificity, positive predictive value (PPV), and negative predictive value (NPV) as well as accuracy were reported for the optimal thresholds. *P* values < 0.05 were considered statistically significant. Statistical analyses were performed using SPSS software (Statistical Package for the Social Sciences, v. 18.0, Chicago, IL).

RESULTS

Table 1 shows the mean ADC values and MRSI ratios for the three different Gleason score categories (GS 3+3, GS 3+4, and GS 4+3). Figures 1 and 2 show the "box and whisker" plots of MRSI ratios and ADC values of three Gleason scores respectively. Figure 3 shows the multivoxel display of a 59-year-old PCa patient showing elevation of Cho and Cr in the right base with corresponding ADC map on the right side. In the MRSI, the mean and SD of (Cho+Cr)/Cit ratio of PCa patients with GS of 3+3 in the peripheral zone was 0.44 ± 0.02 . For GS 3+4 and 4+3 the mean and SD of (Cho+Cr)/Cit ratios were 0.56 ± 0.06 and 0.88 ± 0.11 , respectively. Statistical significance (*P* < 0.05) was found between the Gleason score categories and the metabolite ratio (Cho+Cr/Cit).

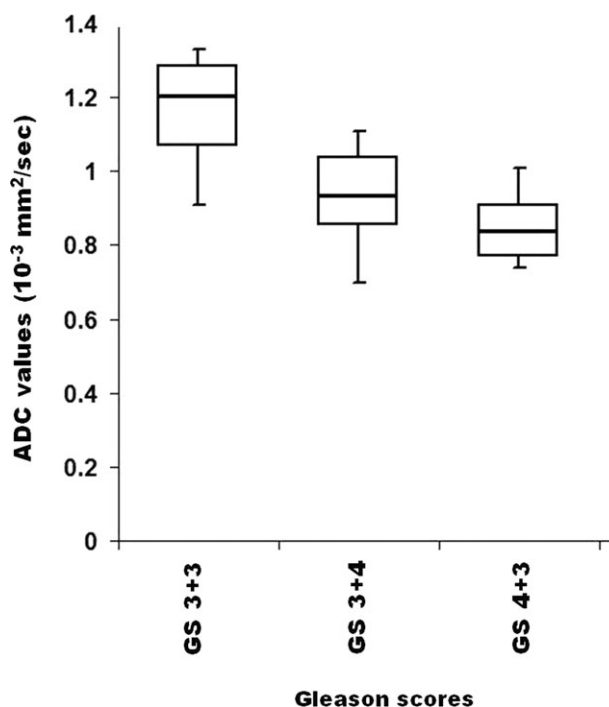


Figure 2. Box-and-whisker plot shows the ADC map of three Gleason scores (GS 3+3, GS 3+4, and GS 4+3).

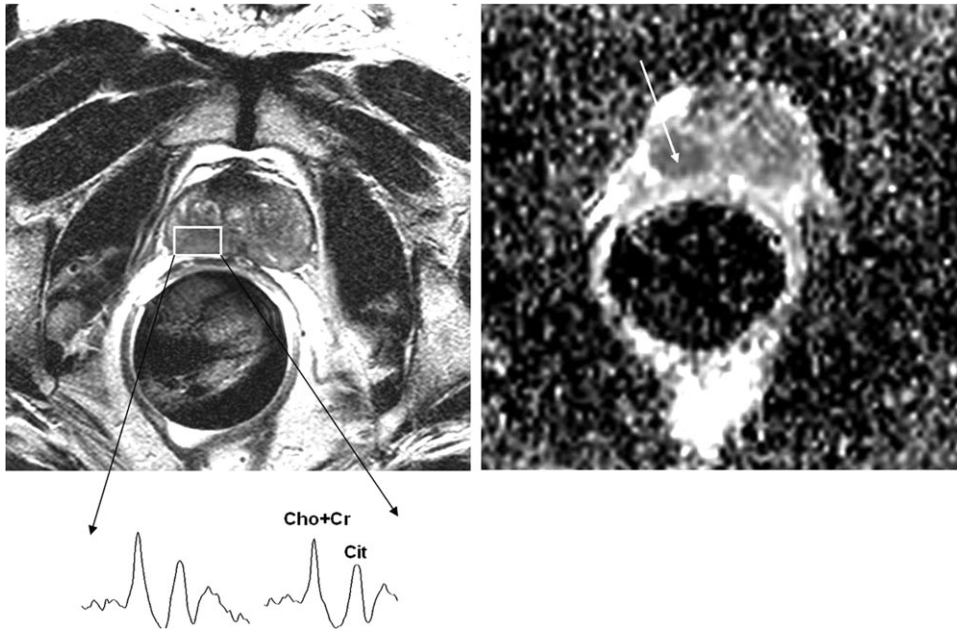


Figure 3. T₂-weighted MRI with MRSI display of a 59-year-old prostate cancer patient with corresponding abnormal ADC (long arrow) map.

The PCa patients with higher Gleason scores tended to show higher metabolic ratios on 3D MRSI. In the DWI of patients with GS 3+3, the mean and SD of the ADC values were $1.13 \pm 0.11 \text{ mm}^2/\text{sec}$ (35 ROIs). For the patients with GS 3+4 and 4+3, the mean and SD of the ADC values were $0.97 \pm 0.10 \text{ mm}^2/\text{sec}$ (48 ROIs) and $0.83 \pm 0.08 \text{ mm}^2/\text{sec}$ (27 ROIs), respectively. The ROIs were drawn to encompass the largest area of PCa without including the tumor margins, the prostate capsule, or the urethra. The areas of ROIs ranged from 4 to 10 mm^2 . The wide range of areas was due to the wide range of prostate carcinomas. Measurements were conducted through a circular ROI on lesions. Statistical significance ($P < 0.05$) was observed between the ADC values and tumor aggressiveness. The ADC intergroup variability between the three different GS falls between 8%–10% and MRSI ratios were 6%–13%. The intravariability of ADC and MRSI were 6% and 9%, respectively. Although there was an overlap among the three GS, statistical significances were observed in metabolites ratio and ADC values. The reason for the overlap may possibly be due to heterogeneity of the PCa.

The results of Spearman correlation analysis are shown in Table 2. We found a strong and statistically significant correlation between each of ADC values and MRSI ratios with Gleason score ($r = -0.665$, $P < 0.001$; and $r = 0.902$, $P < 0.0001$, respectively). There was a weak, but statistically significant correlation,

Table 2
Spearman Rank Correlation to Evaluate Association of Each of the Measures With Gleason Scores and Tumor Volume

Measure	Gleason score		Tumor volume	
	Correlation	<i>P</i>	Correlation	<i>P</i>
ADC	-0.66**	<0.001	0.36*	.018
(Cho+Cr)/Cit	0.90**	<0.001	0.69**	<0.001

**Statistically significant at the 0.001 level.

*Statistically significant at the 0.05 level.

between ADC and tumor volume ($r = 0.366$, $P = 0.018$) and a strong statistically significant correlation between MRSI ratio and tumor volume ($r = 0.694$, $P < 0.001$). In addition, there was a moderate correlation that reached statistical significance between tumor volumes and Gleason scores ($r = 0.360$, $P = 0.021$).

Figure 4 shows the comparison of ROC curves of ADC and MRSI ratios of PCa patients with Gleason scores (Fig. 4A) 3+3 and 3+4, (Fig. 4B) 3+3 and 4+3, (Fig. 4C) 3+4 and 4+3. ROC curve analyses for differentiating GS 3+3 and 3+4 suggest an optimal cutoff value of $1.05 \times 10^{-3} \text{ mm}^2/\text{s}$ for ADC value. This implies a proportion of correctly identified true GS 3+4 cases (sensitivity) of 82.6%, a proportion of correctly identified true GS 3+3 cases (specificity) of 68.2%, a proportion of true GS 3+4 cases (PPV) of 73.1%, and a proportion of true GS 3+3 cases (NPV) of 78.9%. The AUC was 84% with an accuracy of 75.6%. The cutoff values for the MRSI ratios (Cho+Cr)/Cit were 0.49 with sensitivity, specificity and accuracy 96.3%, 90.5%, and 93.8%, respectively. The AUC of the MRSI ratio was the largest (98.2%) in the differentiation between GS 3+3 from 3+4. In the evaluation of GS 3+3 versus 3+4 the MRSI ratios had an AUC of 100%, indicating excellent discrimination compared to AUC of 98.6% for ADC. Similarly, AUC for MRSI ratios for distinguishing GS 3+4 and 4+3 was 100% compared to AUC of 87% for ADC. Detailed results of the ROC curve analyses are given in Table 3, giving the sensitivity, specificity, PPV, NPV, AUC, and accuracy for classifying the cases as GS 3+3 versus 3+4, GS 3+3 versus 4+3, and as GS 3+4 versus 4+3, respectively. For all cases the addition of ADC with MRSI ratio did not improve the classification any further.

DISCUSSION

In the present study we investigated MRSI and DWI of 41 patients with pathologic correlation and confirmed

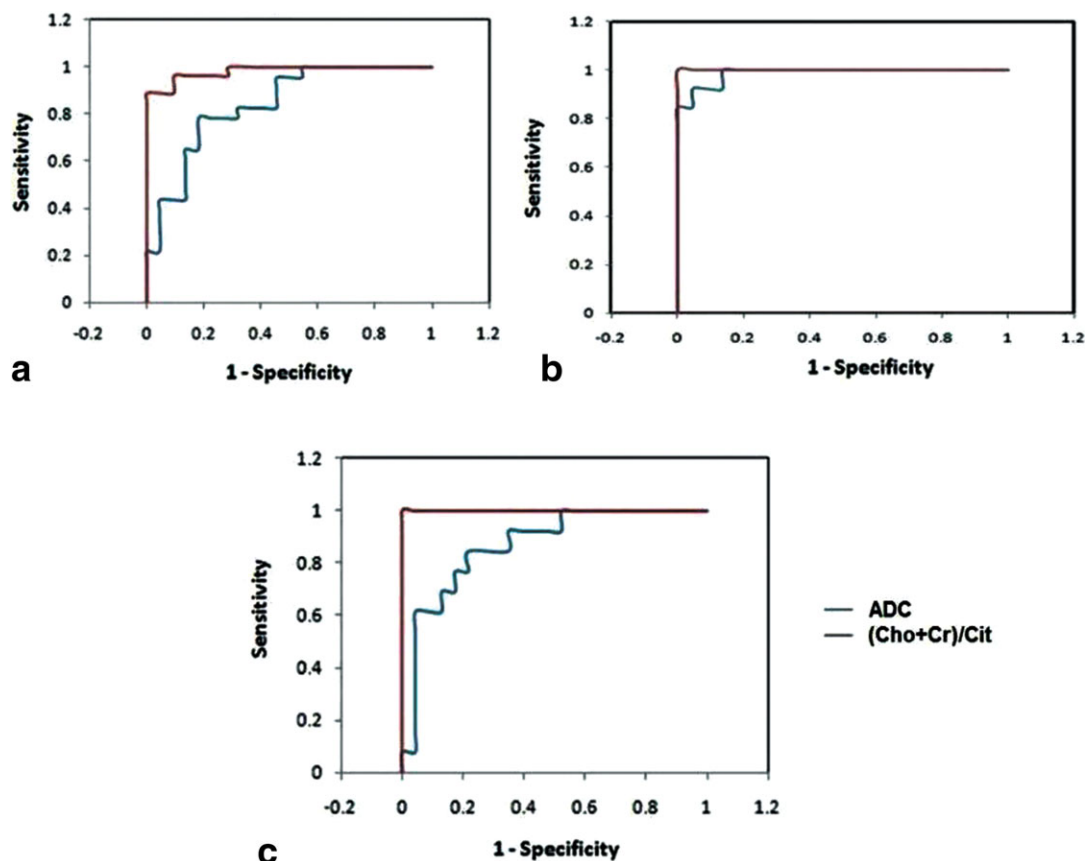


Figure 4. Graph shows ROC curves of ADC and MRSI ratios of prostate cancer patients for differentiation of GS (a) 3+3 from 3+4, (b) 3+3 from 4+3, and (c) 3+4 from 4+3.

that the ratios of (Cho+Cr)/Cit in the lesion are positively correlated with the lesion Gleason scores, with an increase of the Cho level and decrease of the Cit level with rising cancer aggressiveness. This finding is likely clinically relevant, since the surgical Gleason score is used widely in models that are used to predict outcome. Combined MRI and MRSI aids in tumor localization within the peripheral zone (26-28), and preliminary reports of MRSI assessment of tumor aggressiveness have shown promise (29,30). In the last decade, many publications have reported the advantages of MRI and MRSI combining metabolic information directly on the corresponding anatomic display (31,32). The correlation between tumor volume and grade agrees with published reports (33,34).

A significant reduction of ADC values of PCa is well documented (14-16,35-39) and is further supported by our investigation. In our investigation of the relationship between the diffusion characteristics and aggressiveness of PCa, we found that lower ADC values were associated with higher Gleason scores and that ADC values may help to differentiate between low-risk (GS 6) and intermediate-risk (GS 7) prostate cancer if the tumor is visible on DWI. DWI as a functional imaging technique can measure the mobility of water within tissues in addition to depicting tumor size and shape. DWI may detect and localize PCa before the surgery and then may provide qualitative or quantitative information for measuring ADC in patients with PCa after surgery. We found that mean

Table 3
 Measures of Sensitivity, Specificity, PPV, NPV, and Accuracy of ADC and MRSI in Discrimination of GS 3+3 From 3+4, GS 3+3 From 4+3, and GS 3+4 From 4+3 With ROC Curve Analysis

Parameter	CV	Sensitivity, %	Specificity, %	PPV, %	NPV, %	AUC, %	Accuracy, %
ADC							
GS 3+3 vs. GS 3+4	1.05	82.6	68.2	73.1	78.9	84	75.6
GS 3+3 vs. GS 4+3	0.94	92.3	95.5	92.3	95.5	98.6	94.3
GS 3+4 vs. GS 4+3	0.85	69.2	82.6	69.2	82.6	87	77.8
(Cho+Cr)/Cit							
GS 3+3 vs. GS 3+4	0.49	96.3	90.5	92.9	95	98.2	93.8
GS 3+3 vs. GS 4+3	0.75	100	100	100	100	100	100
GS 3+4 vs. GS 4+3	0.75	100	100	100	100	100	100

CV: cutoff value; PPV: positive predictive value; NPV: negative predictive value; AUC: area under the curve.

ADC values were significantly lower and mean metabolite ratios values were significantly higher for malignant PZ tissue with increasing GS. The decrease in ADC values in malignant tissue is attributed to histopathologic characteristics, including hypercellularity, enlargement of nuclei, hyperchromatisms, and angulation of the nuclear contour (40), which result in a reduction of diffusional displacement of water molecules. This study demonstrates the potentials of a combination of DWI, MRSI, and tumor volume of patients with three different Gleason scores using ROC curve analysis.

We have not examined the correlation between biopsy and prostatectomy Gleason score since we do not have the biopsy report for 12 out of 41 patients. In 13 out of 29 (45%) patients the biopsy and prostatectomy Gleason scores were the same. For the remaining 16 patients, five patients with GS 3+3, seven patients with GS 3+4, and four patients with GS 4+3 whose biopsy Gleason scores were different from prostatectomy. The distribution of metabolite values for GS 4+3 is larger than the other group because of a smaller number of subjects. In this study we have not correlated the ADC values with histology data. We observed negative correlation between Gleason scores and ADC values, and positive correlations between Gleason scores and MRSI ratios, and between Gleason scores and tumor volumes.

Most of the studies to date that have assessed the utility of DWI in PCa evaluated lesions within the peripheral zone (PZ). Several studies (41–44) have suggested improvement in tumor detection over T2W, either using DWI alone, or in combination with T2W. Results for comparison between DWI and MRS have been mixed. Chen et al (45) found that DWI (82%) and MRS (84%) had similar sensitivity but DWI had lower specificity (82%) compared with MRS (98%). In contrast, Reinsberg et al (46) instead showed slightly lower sensitivity and specificity rates of DWI compared with that of MRS, particularly when the percentage of tumor within the voxel was smaller.

This study has a few limitations. In the DWI and MRSI in PCa, we included only tumors in the PZ, because heterogeneity in the hyperplastic transition zone of older men limits tumor depiction. However, the majority of tumors are found in the PZ. Our recent work has focused on further investigation using the increased sensitivity advantages of the 3T MRI scanner and the results will be reported later.

In conclusion, combined MRSI and DWI can help in the discrimination of intermediate Gleason grade tumors from low Gleason grade tumors with histopathology as the standard of reference (“gold standard”). This information can guide subsequent definitive management and help to optimize active surveillance programs.

ACKNOWLEDGMENT

The authors thank Mr. Sergio Godinez, Mr. Glen Nyborg, and Ms. Francine Cobla for technical support.

REFERENCES

- Jemal A, Siegel R, Ward E, et al. Cancer statistics, 2009. *CA Cancer J Clin* 2009;59:225–249.
- Stamey TA, Yang N, Hay AR, McNeal JE, Freiha FS, Redwine E. Prostate-specific antigen as a serum marker for adenocarcinoma of the prostate. *N Engl J Med* 1987;317:909–916.
- Smith DS, Catalona WJ. Interexaminer variability of digital rectal examination in detecting prostate cancer. *Urology* 1995;45:70–74.
- Norberg M, Egevad L, Holmberg L, et al. The sextant protocol for ultrasound-guided core biopsies of the prostate underestimates the presence of cancer. *Urology* 1997;50:562–566.
- Chen ME, Troncoso P, Johnston DA, et al. Optimization of prostate biopsy strategy using computer based analysis. *J Urol* 1997;158:2168–2175.
- Gleason DF. Histology grading of prostate cancer: a perspective. *Hum Pathol* 1992;23:273–279.
- Costello LC, Franklin RB. Concepts of citrate production and secretion by prostate. I. Metabolic relationships. *Prostate* 1991;18:25–46.
- Khan T, Beurrig K, Schmitz-Dreager B, et al. Prostatic carcinoma and benign prostatic hyperplasia. *Radiology* 1989;173:847–851.
- Costello LC, Franklin RB. Novel role of zinc in the regulation of prostate citrate metabolism and its implications in prostate cancer. *Prostate* 1998;35:285–296.
- Liang JY, Liu YY, Zou J, et al. Inhibitory effect of zinc on human prostatic carcinoma cell growth. *Prostate* 1999;40:200–207.
- Scheidler J, Hricak H, Vigneron DB, et al. Prostate cancer: localization with three-dimensional proton MR spectroscopic imaging—clinicopathologic study. *Radiology* 1999;213:473–480.
- Swanson MG, Vigneron DB, Tabatabai ZL, et al. Proton HR-MAS spectroscopy and quantitative pathologic analysis of MRI/3D-MRSI-targeted postsurgical prostate tissues. *Magn Reson Med* 2003;50:944–954.
- Yuen JS, Thng CH, Tan PH, et al. Endorectal magnetic resonance imaging and spectroscopy for the detection of tumor foci in men with prior negative transrectal ultrasound prostate biopsy. *J Urol* 2004;171:1482–1486.
- Yamamura J, Salomon G, Buchert R, et al. Magnetic resonance imaging of prostate cancer: diffusion-weighted imaging in comparison with sextant biopsy. *J Comput Assist Tomogr* 2011;35:223–228.
- Hambrock T, Somford DM, Huisman HJ, et al. Relationship between apparent diffusion coefficients at 3.0-T MR imaging and Gleason grade in peripheral zone prostate cancer. *Radiology* 2011;259:453–461.
- Bittencourt LK, Barentsz JO, de Miranda LC, et al. Prostate MRI: diffusion-weighted imaging at 1.5T correlates better with prostatectomy Gleason grades than TRUS-guided biopsies in peripheral zone tumours. *Eur Radiol* 2012;22:468–475.
- Itou Y, Nakanishi K, Narumi Y, Nishizawa Y, Tsukuma H. Clinical utility of apparent diffusion coefficient (ADC) values in patients with prostate cancer: can ADC values contribute to assess the aggressiveness of prostate cancer? *J Magn Reson Imaging* 2011;33:167–172.
- Kirkham APS, Emberton M, Allen C. How good is MRI at detecting and characterising cancer within the prostate? *Eur Radiol* 2006;50:1163–1175.
- Kurhanewicz J, Vigneron DB. Advances in MR spectroscopy of the prostate. *Magn Reson Imaging Clin N Am* 2008;16:697–710.
- Akin O, Sala E, Moskowitz CS, et al. Transition zone prostate: features, detection, localization, and staging at endorectal MR imaging. *Radiology* 2006;239:784–792.
- Fütterer JJ, Engelbrecht MR, Jager GJ, et al. Prostate cancer: comparison of local staging accuracy of pelvic phased-array coil alone versus integrated endorectal-pelvic phased-array coils. Local staging accuracy of prostate cancer using endorectal coil MR imaging. *Eur Radiol* 2007;17:1055–1065.
- Costouros NG, Coakley FV, Westphalen AC, et al. Diagnosis of prostate cancer in patients with elevated prostate-specific antigen level: role of endorectal MRI and MR spectroscopy imaging. *Am J Roentgenol* 2007;188:812–816.
- Westphalen AC, Coakley FV, Gayyum A, et al. Peripheral zone prostate cancer: accuracy of different interpretative approaches with MR and MR spectroscopic imaging. *Radiology* 2008;246:177–184.

24. Sato C, Naganawa S, Nakumara T, et al. Differentiation of non-cancerous tissue and cancer lesions by apparent diffusion coefficient values in transition and peripheral zones of the prostate. *J Magn Reson Imaging* 2005;21:258–262.
25. Mescher M, Tannus A, Johnson MO, et al. Solvent suppression using selective echo dephasing. *J Magn Reson A* 1996;123:226–229.
26. Noworolski SM, Crane JC, Vigneron DB, Kurhanewicz J. A clinical comparison of rigid and inflatable endorectal-coil probes for MRI and 3D MR spectroscopic imaging (MRSI) of the prostate. *J Magn Reson Imaging* 2008;27:1077–1082.
27. Kurhanewicz J, Vigneron DB, Hricak H, et al. Three dimensional H-1 MR spectroscopic imaging of the in situ human prostate with high (0.24–0.7cm³) spatial resolution. *Radiology* 1996;198:795–805.
28. Kumar V, Jagannathan NR, Kumar R, et al. Potential of (1)HMR spectroscopic imaging to segregate patients who are likely to show malignancy of the peripheral zone of the prostate on biopsy. *J Magn Reson Imaging* 2009;30:842–848.
29. Giusti S, Caramella D, Fruzzetti E, et al. Peripheral zone prostate cancer. Pre-treatment evaluation with MR and 3D ¹HMR spectroscopic imaging: correlation with pathologic findings. *Abdom Imaging* 2010;35:757–763.
30. Zakian KL, Sircar K, Kleinman S, et al. Correlation of proton MR spectroscopic imaging with Gleason score based on step section radical prostatectomy (abstract). *Radiology* 2002;225:1525.
31. Chen ME, Troncoso P, Johnston DA, et al. Functional MR imaging of prostate cancer. *Radiographics* 2007;27:63–75.
32. Kobus T, Hambroek T, Hulsbergen-van de Kaa CA, et al. In vivo assessment of prostate cancer aggressiveness using magnetic resonance spectroscopic imaging at 3 T with an endorectal coil. *Eur Urol* 2011;60:1074–1080.
33. Augustin H, Hammerer PG, Graefen M, et al. Characterisation of biomolecular profiles in primary high-grade prostate cancer treated by radical prostatectomy. *J Cancer Res Clin Oncol* 2003;129:662–668.
34. Eichelberger LE, Koch MO, Daggy JK, et al. Predicting tumor volume in radical prostatectomy specimens from patients with prostate cancer. *Am J Clin Pathol* 2003;120:386–391.
35. Kumar V, Jagannathan NR, Kumar R, et al. Apparent diffusion coefficient of the prostate in men prior to biopsy: determination of a cut-off value to predict malignancy of the peripheral zone. *NMR Biomed* 2007;20:505–511.
36. Tanimoto A, Nakashima J, Kohno H, et al. Prostate cancer screening: the clinical value of diffusion-weighted imaging and dynamic MR imaging in combination with T2-weighted imaging. *J Magn Reson Imaging* 2007;25:146–152.
37. DeSouza NM, Reinsberg SA, Scurr ED, et al. Magnetic resonance imaging in prostate cancer: the value of apparent diffusion coefficients for identifying malignant nodules. *Br J Radiol* 2007;80:90–95.
38. Shimofusa R, Fujimoto H, Akamata H, et al. Diffusion-weighted imaging of prostate cancer. *J Comput Assist Tomogr* 2005;29:149–153.
39. Hosseinzadeh K, Schwarz SD. Endorectal diffusion-weighted imaging in prostate cancer to differentiate malignant and benign peripheral zone tissue. *J Magn Reson Imaging* 2004;20:654–661.
40. Anderson JR. *Muir's textbook of pathology*. London: Edward Arnold; 1985.
41. Mazaheri Y, Hricak H, Fine SW, et al. Prostate tumor volume measurement with combined T2-weighted imaging and diffusion-weighted MR: correlation with pathologic tumor volume. *Radiology* 2009;252:449–457.
42. Miao H, Fukatsu H, Ishigaki T. Prostate cancer detection with 3-T MRI: comparison of diffusion-weighted and T2-weighted imaging. *Eur J Radiol* 2007;61:297–302.
43. Yoshimitsu K, Kiyoshima K, Irie H, et al. Usefulness of apparent diffusion coefficient map in diagnosing prostate carcinoma: correlation with stepwise histopathology. *J Magn Reson Imaging* 2008;27:132–139.
44. Kim CK, Choi D, Park BK, et al. Diffusion weighted MR imaging for the evaluation of SVI in prostate cancer: initial results. *J Magn Reson Imaging* 2008;28:963–969.
45. Chen M, Dang HD, Wang JY, et al. Prostate cancer detection: comparison of T2-weighted imaging, diffusion-weighted imaging, proton magnetic resonance spectroscopic imaging, and the three techniques combined. *Acta Radiol* 2008;49:602–610.
46. Reinsberg SA, Payne GS, Riches SF, et al. Combined use of diffusion weighted MRI and 1H MR spectroscopy to increase accuracy in prostate cancer detection. *AJR Am J Roentgenol* 2007;188:91–98.

Research Article

Correlation of Gleason Scores with Diffusion-Weighted Imaging Findings of Prostate Cancer

Rajakumar Nagarajan,¹ Daniel Margolis,¹ Steven Raman,¹ Ke Sheng,²
Christopher King,² Robert Reiter,³ and M. Albert Thomas¹

¹ Department of Radiological Sciences, David Geffen School of Medicine, University of California, Los Angeles, CA 90095-1721, USA

² Department of Radiation Oncology, David Geffen School of Medicine, University of California, Los Angeles, CA 90095-1721, USA

³ Department of Urology, David Geffen School of Medicine, University of California, Los Angeles, CA 90095-1721, USA

Correspondence should be addressed to M. Albert Thomas, athomas@mednet.ucla.edu

Received 15 August 2011; Revised 5 October 2011; Accepted 5 October 2011

Academic Editor: Jack Schalken

Copyright © 2012 Rajakumar Nagarajan et al. This is an open access article distributed under the Creative Commons Attribution License, which permits unrestricted use, distribution, and reproduction in any medium, provided the original work is properly cited.

The purpose of our study was to compare the apparent diffusion coefficient (ADC) derived from diffusion-weighted imaging (DWI) of prostate cancer (PCa) patients with three classes of pathological Gleason scores (GS). Patients whose GS met these criteria (GS 3 + 3, GS 3 + 4, and GS 4 + 3) were included in this study. The DWI was performed using b values of 0, 50, and 400 s/mm² in 44 patients using an endorectal coil on a 1.5T MRI scanner. The apparent diffusion coefficient (ADC) values were calculated from the DWI data of patients with three different Gleason scores. In patients with a high-grade Gleason score (4 + 3), the ADC values were lower in the peripheral gland tissue, pathologically determined as tumor compared to low grade (3 + 3 and 3 + 4). The mean and standard deviation of the ADC values for patients with GS 3 + 3, GS 3 + 4, and GS 4 + 3 were 1.135 ± 0.119 , 0.976 ± 0.103 and 0.831 ± 0.087 mm²/sec. The ADC values were statistically significant ($P < 0.05$) between the three different scores with a trend of decreasing ADC values with increasing Gleason scores by one-way ANOVA method. This study shows that the DWI-derived ADC values may help differentiate aggressive from low-grade PCa.

1. Introduction

Prostate cancer (PCa) is the most common malignancy among men in the USA, with an estimated 217,730 new cases and 32,050 PCa-related deaths in 2010 [1]. The incidence of PCa increases with age, and it is very uncommon in men younger than 50 years old. With greater longevity and increased awareness of the disease leading to more men requesting screening, it is to be expected that there will be an increase in the number of patients diagnosed with PCa in the future. Most men diagnosed with PCa ultimately survive the disease and die of other causes. The overall 5-year survival rate is 99% for all stages, but only 34% when there are distant metastases [2]. The aim of PCa management is to identify, treat, and cure patients with aggressive disease that may prove fatal but to avoid overtreatment of those in whom the disease is unlikely to be life threatening. Most patients diagnosed with PCa have localized disease confined to the

prostate. A small number with high-grade tumors will progress to develop local, extracapsular tumor extension and distant metastases.

Prostate tumors are graded according to their pathological appearance with a Gleason score (GS), which represents the sum of the dominant and subdominant histological patterns (grades). High GSs indicate aggressive tumors with increased potential for local and distant spread; Gleason grading has been shown to provide a spectrum of risk for all patients [3]. Magnetic resonance imaging (MRI) provides incremental value to clinical findings in staging patients of intermediate risk. For example, organ-confined disease implies that the patient may benefit from local therapy such as surgery [4]. MRI is more accurate than either digital rectal examination (DRE) or transrectal ultrasound (TRUS) biopsy in preoperative anatomical localization of PCa [5]. The sensitivity and specificity of T₂-weighted imaging for PCa vary widely due to differences in imaging techniques,

reference standards, criteria for defining disease involvement on MRI, and interobserver variability [6]. In a meta-analysis by Sonnad et al. T₂-weighted imaging showed a maximum joint sensitivity and specificity rate of 74% for the staging of PCa [7]. In T₂-weighted imaging, regions of PCa show decreased signal intensity relative to normal peripheral (PZ) tissue because of increased cell density and a loss of prostatic ducts [8]. This finding is nonspecific, however, because other diseases such as prostatitis or hyperplasia can also cause low signal intensity in T₂-weighted imaging [9–12].

Diffusion-weighted imaging (DWI) is another MR-based technique that probes functional characteristics of tissues. The clinical success of DWI has led to a broadening application in the prostate gland. Rapid changes in diffusion properties can be identified by calculating the apparent diffusion coefficient (ADC). Dickinson et al. [13] showed the standardizing multiparametric magnetic resonance imaging (mpMRI) for PCa detection, localization, and characterization. The use of DWI as a tool for the evaluation and management of prostatic cancer has grown steadily in the past decades [14–16]. The purpose of the study was to record DWI and to compare ADC values derived from DWI in PCa patients with three different Gleason scores (3 + 3, 3 + 4, and 4 + 3).

2. Materials and Methods

A total of 44 clinically localized PCa patients who underwent radical retropubic prostatectomy between January, 2007 and May, 2008 were selected for this study. The entire protocol was approved by the institutional review board (IRB), and an informed consent was obtained from each human subject. The ages of the patients ranged from 47 to 75 years, and the patients fell into three different groups by surgery GS: 3 + 3 (mean ± SD, 60.1 ± 6.7 years), 3 + 4 (mean ± SD, 58.1 ± 4.2 years), and 4 + 3 (mean ± SD, 60.3 ± 3.9 years). The mean prostate-specific antigen (PSA) value for the patients with GS 3 + 3, GS 3 + 4, and GS 4 + 3, respectively, were 5.0 ng/mL, 6.8 ng/mL, and 7.4 ng/mL.

All patients underwent prostate imaging with an endorectal coil on a 1.5 Tesla Avanto-Tim MRI scanner with high-performance gradients (Siemens Medical Solutions, Erlangen, Germany). Sequences included axial turbo spin-echo (TSE) T₂-weighted imaging through the prostate and seminal vesicles (TR/TE, 3800/101 ms; slice thickness, 3 mm; no interslice gap; field of view (FOV), 140 mm, matrix 205 × 256, slice thickness 3 mm, interslice gap 0 mm, echo-train number 32, turbo factor 13). In addition, echo-planar diffusion-weighted sequences sensitized in three orthogonal planes (TR/TE 2000/83 ms, bandwidth 1396 Hz in the EPI frequency direction) with *b* values of 0, 50, 400 s/mm² were obtained at the same slice positions as the axial T₂-weighted images. Twelve 4-mm-thick slices with no interslice gap (27 cm FOV) with three averages provided coverage of the prostate with an image acquisition time of less than a minute. Isotropic ADC maps were generated with the system software using all *b* values and taking an average value for the two directions of diffusion sensitization.

MR Images were initially reviewed without clinical information, but the final report was generated after the clinical information was reviewed. The histology was reviewed by an experienced pathologist. The edge and the contour characteristics of the lesions were defined using the same slices on which regions-of-interest (ROI) analyses were performed. ROIs were drawn independently on the ADC maps, and differences in measurement were resolved by consensus. ROIs were drawn in the tumor PZ of all the 44 PCa patients. ADCs were calculated for all slices by

$$\text{ADC} = -\frac{\ln(S_1 - S_0)}{(b_1 - b_0)} \text{ mm}^2/\text{s}, \quad (1)$$

where *S*₁ is the signal intensity of a voxel after application of a diffusion gradient and *S*₀ is the echo magnitude without diffusion gradients applied (*b* = 0 s/mm²). Diffusion sensitivity is determined by the difference between *b*₁ and *b*₀. If multiple tumors were present in the peripheral zone, the average ADC value was recorded for each lesion. The MRI sections and histological slices were matched on the basis of the sextant level, anterior/posterior, and peripheral/central (transitional).

At the time of these examinations, other sequences performed as part of the routine prostate MRI protocol at our institution but not assessed in this study included sagittal and coronal TSE T₂-weighted imaging sequences through the prostate and seminal vesicles.

3. Statistical Analysis

Statistical analyses were performed to assess the statistical differences between ADC values for the three different Gleason scores (GS 3 + 3, GS 3 + 4, and GS 4 + 3) using one-way analysis of variance (ANOVA) with SPSS software package assuming parameters were normally distributed. A *P* value of less than 0.05 was considered to indicate a statistically significant difference. To explore for any relationship between the ADC value, tumor volumes, and the Gleason score, Pearson correlation was performed on the data. Also, analysis of covariance (ANCOVA) was done on ADC values of different Gleason scores with tumor volume as a covariate to see its effect.

4. Results

The patients mean and standard deviation (SD) of age and PSA and ADC values for tumor PZ regions of three Gleason scores are shown in Table 1. Figure 1(a) shows the T₂-weighted MRI of a 68-year-old PCa patient with GS 3 + 4 and Figure 1(b), corresponding ADC map with low signal on the left base PZ. Figure 2 illustrates a box plot of ADC values for PCa in the peripheral zone tissue categorized by the three Gleason scores. In 13 patients with GS 3 + 3, the (mean ± SD) ADC value was 1.135 ± 0.119 mm²/sec using 32 ROIs. In 22 patients with GS 3 + 4, the (mean ± SD) ADC value was 0.976 ± 0.103 mm²/sec using 52 ROIs. In 9 patients with GS 4 + 3, the (mean ± SD) ADC value was 0.831 ± 0.087 mm²/sec using 24 ROIs. Although a statistically significant difference

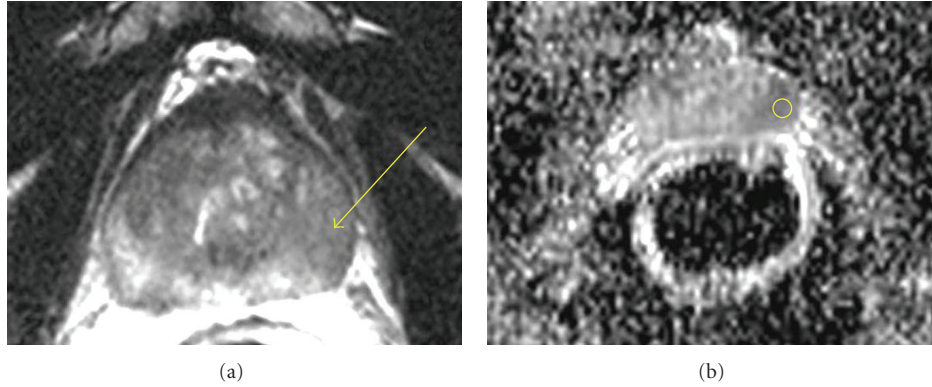


FIGURE 1: (a) T₂-weighted MRI of 68 yo prostate cancer patient with GS 3 + 4 and (b) corresponding ADC map with low signal on the left base PZ.

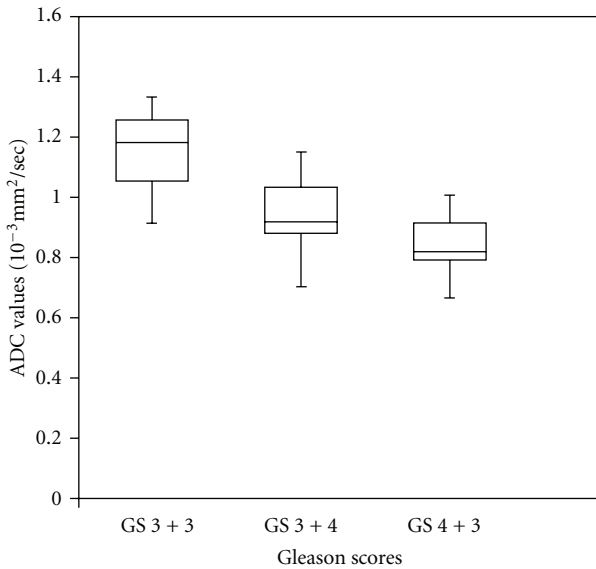


FIGURE 2: Box-Whisker plots of ADC values of Gleason score (GS) 3 + 3, (GS) 3 + 4 and (GS) 4 + 3 patients. The center horizontal line indicates the median.

TABLE 1: Patient clinical information and ADC values.

Gleason scores	Age mean ± SD	PSA mean ± SD (ng/mL)	ADC values mean ± SD (mm ² /sec)
3 + 3 (n = 13)	60.1 ± 6.7	5.0 ± 2.8	1.135 ± 0.119
3 + 4 (n = 22)	58.1 ± 4.2	6.8 ± 1.7	0.976 ± 0.103
4 + 3 (n = 9)	60.3 ± 3.9	7.4 ± 2.8	0.831 ± 0.087
P value	NS	NS	<0.05***

NS—Nonsignificant
 ***—Significant.

existed between the three groups ($P < 0.05$), a certain degree of overlap between tissue types was evident. There was no statistical significance between the PSA and patients ages with three different Gleason scores.

We did not have the biopsy report for 14 patients out of 44 patients. Out of which 15 patients whose biopsy and prostatectomy Gleason scores were the same. For the remaining 15 patients, We had four patients with GS 3 + 3, eight patients with GS 3 + 4, and 3 patients with GS 4 + 3 whose biopsy Gleason scores were different from prostatectomy. Hence, we have not done the correlation between biopsy and prostatectomy Gleason scores. Out of 44 patients, in 35 patients (GS 3 + 3 ($n = 13$), GS 3 + 4 ($n = 13$), and GS 4 + 3 ($n = 9$)) tumors were detected by the DWI technique. Nine patients (GS 3 + 4 ($n = 9$)) were missed by the MRI technique. To evaluate the association between ADC value, tumor volumes, and the Gleason grade, all the ADC values and tumor volumes were first summarized at the individual patient level, followed by applying Pearson's correlation coefficients. We observed negative correlation between Gleason score and ADC values and positive correlation between Gleason score and tumor volume. In the ANCOVA analysis, the results were statistically significant ($P = 0.0001$) between the Gleason score and ADC values.

5. Discussion

To increase the accuracy of MRI, a number of authors have used special techniques to study a particular characteristic of the prostate tumor and surrounding tissues such as dynamic contrast-enhanced (DCE) MRI [17–19] and MR spectroscopy (MRS) [20–24]. MR spectroscopy requires a substantially longer examination time than DWI, and, additionally, shimming process and placement of saturation bands during the examination are time consuming. For evaluation of MRS, baseline correction and phase correction have to be performed in some cases.

DWI is the only functional imaging technique that is able to assess molecular diffusion in vivo and provides information about biophysical properties of tissues such as cell organization, density, and microstructure [25]. DWI may be helpful in differentiating high-risk patients from those at low and intermediate risks, since there is a significant correlation between the ADC values from patients with three different Gleason scores. The patients with the Gleason score of 4 + 3

have a higher likelihood of biochemical recurrence, particularly for the increasing proportion of patients with organ-confined disease after radical prostatectomy than those with 3 + 4 as reported by Sakr et al. [26]. Also, our results showed decreased ADC values in patients with GS 4 + 3 than those with GS 3 + 4 significantly ($P < 0.05$). This may be useful to assess the aggressiveness of the PCa. The sensitivity of DWI is better in the PZ than the central gland [27]. DWI has also been shown to be helpful in the identification of PCa in patients with previous negative biopsies and persistently elevated PSA [28].

McNeal et al. [29] reported that 65% of prostate cancers arise in the PZ and up to 30% arise in the transition zone (TZ). The transrectal MRI is generally considered less specific for use in the evaluation of TZ cancers because of the heterogeneously low T_2 signal intensity in normal TZ [30], and the presence of benign prostatic hyperplasia in TZ [31, 32]. The endorectal coil offers poor signal sensitivity when it comes to the TZ. Hosseinzadeh and Schwarz [33] successfully investigated T_2 relaxation rates and diffusion-weighted images of the human prostate using an endorectal coil. DWI can provide valuable cellular information about tissue in addition to the conventional T_1 and T_2 -weighted imaging [34–38]. In this present study, ADC values show a decreasing trend with increasing Gleason scores. The calculated ADCs for cancer in the PZ were consistent with those previously reported studies [25, 39–41]. These findings suggest that measurement of ADC may provide an additional feature that could further increase the specificity of diagnosis for PCa. The variation in reported ADC values could be due to a number of physiologic factors (e.g., age tumor size) as well as technical factors (e.g., variations in acquisition parameters, inhomogeneous signal reception using the endorectal MRI coil, and postprocessing methods).

Our study suffered some limitations. We analyzed cancer only in the PZ, where most cancers occur. DWI itself also has some limitations as this sequence is affected by magnetic susceptibility, resulting in spatial distortion and signal loss. Moreover, there is no consensus on the optimal b value for DWI of the prostate.

In conclusion, this study shows that the DWI correlates with pathological Gleason scores. DWI-acquired ADC values are a very potential measure to delineate prostate carcinoma from the PZ and are able to predict the presence of low, and high-grade components in PCa with great accuracy. The ADC values derived from the 1.5 T diffusion-weighted MRI demonstrate tumor aggressiveness and could be of future use in treatment decisions and in patient followup in active surveillance.

Acknowledgments

This work was partially supported by the Department of Defense (DOD) prostate cancer research program IDEA Grant (no. W81XWH-11-1-0248). The authors acknowledge Dr. Jon Furuyama for reading this paper and technical support of Mr. Sergio Godinez, Mr. Glen Nyborg, and Ms. Francine Cobla.

References

- [1] A. Jemal, R. Siegel, J. Xu, and E. Ward, "Cancer statistics, 2010," *CA: Cancer Journal for Clinicians*, vol. 60, no. 5, pp. 277–300, 2010.
- [2] V. Kundra, P. M. Silverman, S. F. Matin, and H. Choi, "Imaging in oncology from the University of Texas M. D. Anderson Cancer Center: diagnosis, staging, and surveillance of prostate cancer," *American Journal of Roentgenology*, vol. 189, no. 4, pp. 830–844, 2007.
- [3] P. C. Albertsen, J. A. Hanley, D. F. Gleason, and M. J. Barry, "Competing risk analysis of men aged 55 to 74 years at diagnosis managed conservatively for clinically localized prostate cancer," *Journal of the American Medical Association*, vol. 280, no. 11, pp. 975–980, 1998.
- [4] L. Wang, M. Mullerad, H. N. Chen et al., "Prostate cancer: incremental value of endorectal MR imaging findings for prediction of extracapsular extension," *Radiology*, vol. 232, no. 1, pp. 133–139, 2004.
- [5] M. Mullerad, H. Hricak, K. Kuroiwa et al., "Comparison of endorectal magnetic resonance imaging, guided prostate biopsy and digital rectal examination in the preoperative anatomical localization of prostate cancer," *Journal of Urology*, vol. 174, no. 6, pp. 2158–2163, 2005.
- [6] Y. Mazaheri, A. Shukla-Dave, A. Muellner, and H. Hricak, "MR imaging of the prostate in clinical practice," *Magnetic Resonance Materials in Physics, Biology and Medicine*, vol. 21, no. 6, pp. 379–392, 2008.
- [7] S. S. Sonnad, C. P. Langlotz, and J. S. Schwartz, "Accuracy of MR imaging for staging prostate cancer: a meta-analysis to examine the effect of technologic change," *Academic Radiology*, vol. 8, no. 2, pp. 149–157, 2001.
- [8] K. K. Yu and H. Hricak, "Imaging prostate cancer," *Radiologic Clinics of North America*, vol. 38, no. 1, pp. 59–85, 2000.
- [9] H. Hricak, S. White, D. Vigneron et al., "Carcinoma of the prostate gland: MR imaging with pelvic phased-array coils versus integrated endorectal-pelvic phased-array coils," *Radiology*, vol. 193, no. 3, pp. 703–709, 1994.
- [10] L. E. Quint, J. S. Van Erp, P. H. Bland et al., "Prostate cancer: correlation of MR images with tissue optical density at pathologic examination," *Radiology*, vol. 179, no. 3, pp. 837–842, 1991.
- [11] K. Lovett, M. D. Rifkin, P. A. McCue, and H. Choi, "MR imaging characteristics of noncancerous lesions of the prostate," *Journal of Magnetic Resonance Imaging*, vol. 2, no. 1, pp. 35–39, 1992.
- [12] S. White, H. Hricak, R. Forstner et al., "Prostate cancer: effect of postbiopsy hemorrhage on interpretation of MR images," *Radiology*, vol. 195, no. 2, pp. 385–390, 1995.
- [13] L. Dickinson, H. U. Ahmed, C. Allen et al., "Magnetic resonance imaging for the detection, localisation, and characterisation of prostate cancer: recommendations from a European consensus meeting," *European Urology*, vol. 59, no. 4, pp. 477–494, 2011.
- [14] L. K. Bittencourt, J. O. Barentsz, L. C. D. de Miranda, and E. L. Gasparetto, "Prostate MRI: diffusion-weighted imaging at 1.5T correlates better with prostatectomy Gleason grades than TRUS-guided biopsies in peripheral zone tumours," *European Radiology*. In press.
- [15] J. Yamamura, G. Salomon, R. Buchert et al., "Magnetic resonance imaging of prostate cancer: diffusion-weighted imaging in comparison with sextant biopsy," *Journal of Computer Assisted Tomography*, vol. 35, no. 2, pp. 223–228, 2011.

- [16] T. Hambrock, D. M. Somford, H. J. Huisman et al., "Relationship between apparent diffusion coefficients at 3.0-T mr imaging and gleason grade in peripheral zone prostate cancer," *Radiology*, vol. 259, no. 2, pp. 453–461, 2011.
- [17] J. O. Barentsz, M. Engelbrecht, G. J. Jager et al., "Fast dynamic gadolinium-enhanced MR imaging of urinary bladder and prostate cancer," *Journal of Magnetic Resonance Imaging*, vol. 10, no. 3, pp. 295–304, 1999.
- [18] J. T. Heverhagen, H. Von Tengg-Kobligk, K. T. Baudendistel et al., "Benign prostate hyperplasia: evaluation of treatment response with DCE MRI," *Magnetic Resonance Materials in Physics, Biology and Medicine*, vol. 17, no. 1, pp. 5–11, 2004.
- [19] N. Hara, M. Okuizumi, H. Koike, M. Kawaguchi, and V. Bilim, "Dynamic contrast-enhanced magnetic resonance imaging (DCE-MRI) is a useful modality for the precise detection and staging of early prostate cancer," *Prostate*, vol. 62, no. 2, pp. 140–147, 2005.
- [20] R. Dhingsa, A. Qayyum, F. V. Coakley et al., "Prostate cancer localization with endorectal MR imaging and MR spectroscopic imaging: effect of clinical data on reader accuracy," *Radiology*, vol. 230, no. 1, pp. 215–220, 2004.
- [21] F. V. Coakley, S. T. Hui, A. Qayyum et al., "Endorectal MR imaging and MR spectroscopic imaging for locally recurrent prostate cancer after external beam radiation therapy: preliminary experience," *Radiology*, vol. 233, no. 2, pp. 441–448, 2004.
- [22] P. Swindle, S. McCredie, P. Russell et al., "Pathologic characterization of human prostate tissue with proton MR spectroscopy," *Radiology*, vol. 228, no. 1, pp. 144–151, 2003.
- [23] K. L. Zakian, S. Eberhardt, H. Hricak et al., "Transition zone prostate cancer: metabolic characteristics at 1H MR spectroscopic imaging—initial results," *Radiology*, vol. 229, no. 1, pp. 241–247, 2003.
- [24] F. G. Claus, H. Hricak, and R. R. Hattery, "Pretreatment evaluation of prostate cancer: role of MR imaging and 1H MR spectroscopy," *Radiographics*, vol. 24, pp. S167–S180, 2004.
- [25] P. Gibbs, D. J. Tozer, G. P. Liney, and L. W. Turnbull, "Comparison of quantitative T2 mapping and diffusion-weighted imaging in the normal and pathologic prostate," *Magnetic Resonance in Medicine*, vol. 46, no. 6, pp. 1054–1058, 2001.
- [26] W. A. Sakr, M. V. Tefilli, D. J. Grignon et al., "Gleason score 7 prostate cancer: a heterogeneous entity? Correlation with pathologic parameters and disease-free survival," *Urology*, vol. 56, no. 5, pp. 730–734, 2000.
- [27] M. A. Haider, T. H. van der Kwast, J. Tanguay et al., "Combined T2-weighted and diffusion-weighted MRI for localization of prostate cancer," *American Journal of Roentgenology*, vol. 189, no. 2, pp. 323–328, 2007.
- [28] B. K. Park, H. M. Lee, C. K. Kim, H. Y. Choi, and J. W. Park, "Lesion localization in patients with a previous negative transrectal ultrasound biopsy and persistently elevated prostate specific antigen level using diffusion-weighted imaging at three tesla before rebiopsy," *Investigative Radiology*, vol. 43, no. 11, pp. 789–793, 2008.
- [29] J. E. McNeal, E. A. Redwine, F. S. Freiha, and T. A. Stamey, "Zonal distribution of prostatic adenocarcinoma. Correlation with histologic pattern and direction of spread," *American Journal of Surgical Pathology*, vol. 12, no. 12, pp. 897–906, 1988.
- [30] O. Akin, E. Sala, C. S. Moskowitz et al., "Transition zone prostate cancers: features, detection, localization, and staging at endorectal MR imaging," *Radiology*, vol. 239, no. 3, pp. 784–792, 2006.
- [31] S. Ikonen, L. Kivisaari, P. Tervahartiala, T. Vehmas, K. Taari, and S. Rannikko, "Prostatic MR imaging: accuracy in differentiating cancer from other prostatic disorders," *Acta Radiologica*, vol. 42, no. 4, pp. 348–354, 2001.
- [32] M. L. Schiebler, J. E. Tomaszewski, M. Bezzi et al., "Prostatic carcinoma and benign prostatic hyperplasia: correlation of high-resolution MR and histopathologic findings," *Radiology*, vol. 172, no. 1, pp. 131–137, 1989.
- [33] K. Hosseinzadeh and S. D. Schwarz, "Endorectal diffusion-weighted imaging in prostate cancer to differentiate malignant and benign peripheral zone tissue," *Journal of Magnetic Resonance Imaging*, vol. 20, no. 4, pp. 654–661, 2004.
- [34] K. J. Macura, "Multiparametric magnetic resonance imaging of the prostate: current status in prostate cancer detection, localization, and staging," *Seminars in Roentgenology*, vol. 43, no. 4, pp. 303–313, 2008.
- [35] T. L. Chenevert, L. D. Stegman, J. M. G. Taylor et al., "Diffusion magnetic resonance imaging: an early surrogate marker of therapeutic efficacy in brain tumors," *Journal of the National Cancer Institute*, vol. 92, no. 24, pp. 2029–2036, 2000.
- [36] T. L. Chenevert, C. R. Meyer, B. A. Moffat et al., "Diffusion MRI: a new strategy for assessment of cancer therapeutic efficacy," *Molecular Imaging*, vol. 1, no. 4, pp. 336–343, 2002.
- [37] A. M. Herneth, K. Friedrich, C. Weidekamm et al., "Diffusion weighted imaging of bone marrow pathologies," *European Journal of Radiology*, vol. 55, no. 1, pp. 74–83, 2005.
- [38] M. A. Jacobs, E. H. Herskovits, and H. S. Kim, "Uterine fibroids: diffusion-weighted MR imaging for monitoring therapy with focused ultrasound surgery—preliminary study," *Radiology*, vol. 236, no. 1, pp. 196–203, 2005.
- [39] N. M. deSouza, S. A. Reinsberg, E. D. Scurr, J. M. Brewster, and G. S. Payne, "Magnetic resonance imaging in prostate cancer: the value of apparent diffusion coefficients for identifying malignant nodules," *British Journal of Radiology*, vol. 80, no. 950, pp. 90–95, 2007.
- [40] R. Shimofusa, H. Fujimoto, H. Akamata et al., "Diffusion-weighted imaging of prostate cancer," *Journal of Computer Assisted Tomography*, vol. 29, no. 2, pp. 149–153, 2005.
- [41] C. Sato, S. Naganawa, T. Nakamura et al., "Differentiation of noncancerous tissue and cancer lesion by apparent diffusion coefficient values in transition and peripheral zones of the prostate," *Journal of Magnetic Resonance Imaging*, vol. 21, no. 3, pp. 258–262, 2005.

Use of MR Imaging to Determine Preservation of the Neurovascular Bundles at Robotic-assisted Laparoscopic Prostatectomy¹

Timothy D. McClure, MD
 Daniel J. A. Margolis, MD
 Robert E. Reiter, MD
 James W. Sayre, PhD
 M. Albert Thomas, PhD
 Rajakumar Nagarajan, PhD
 Mittul Gulati, MD
 Steven S. Raman, MD

Purpose:

To determine whether findings at preoperative endorectal coil magnetic resonance (MR) imaging influence the decision to preserve neurovascular bundles and the extent of surgical margins in robotic-assisted laparoscopic prostatectomy (RALP).

Materials and Methods:

This study was approved by the investigational review board and was compliant with the HIPAA; the requirement to obtain informed consent was waived. The authors prospectively evaluated 104 consecutive men with biopsy-proved prostate cancer who underwent preoperative endorectal coil MR imaging of the prostate and subsequent RALP. MR imaging was performed at 1.5 T between January 2004 and April 2008 and included T2-weighted imaging ($n = 104$), diffusion-weighted imaging ($n = 88$), dynamic contrast-enhanced imaging ($n = 51$), and MR spectroscopy ($n = 91$). One surgeon determined the planned preoperative extent of resection bilaterally on the basis of clinical information and then again after review of the final MR imaging report. The differences in the surgical plan before and after review of the MR imaging report were determined and compared with the actual surgical and pathologic results by using logistic regression analysis. Continuous and ranked variables underwent Pearson and Spearman analysis.

Results:

After review of MR imaging results, the initial surgical plan was changed in 28 of the 104 patients (27%); the surgical plan was changed to a nerve-sparing technique in 17 of the 28 patients (61%) and to a non-nerve-sparing technique in 11 (39%). Seven of the 104 patients (6.7%) had positive surgical margins. In patients whose surgical plan was changed to a nerve-sparing technique, there were no positive margins on the side of the prostate with a change in treatment plan.

Conclusion:

Preoperative prostate MR imaging data changed the decision to use a nerve-sparing technique during RALP in 27% of patients in this series.

© RSNA, 2012

¹From the Department of Radiology, David Geffen School of Medicine at UCLA, 200 Medical Plaza, #165-43, MC 695224, Los Angeles, CA 90095-6952. Received January 6, 2011; revision requested February 22; revision received June 27; accepted July 29; final version accepted September 26. Address correspondence to D.J.A.M. (e-mail: daniel.margolis@ucla.edu).

Prostate cancer is the most common noncutaneous cancer diagnosed in American men (1). One standard of care for therapy of organ-confined cancers has been the radical retropubic prostatectomy, which carries a substantial risk of morbidity—including incontinence and impotence. A variety of newer “nerve-sparing” open and laparoscopic techniques have been developed, purportedly to address this issue (2), including robotic-assisted laparoscopic prostatectomy (RALP) (3). RALP provides improved visualization of the surgical field and improved instrument control when compared with other techniques. However, surgeons performing RALP lack tactile (haptic) feedback, upon which they traditionally rely to determine the extent of resection (4). Lack of tactile sensation may compromise a surgeon’s ability to appropriately evaluate potential involvement of the neurovascular bundles by prostatic adenocarcinoma. Surgeons must balance the extent of resection proportionate to the volume of cancer with the probability of extracapsular infiltration. Overly aggressive resections risk impotence and incontinence, but overly conservative resections risk positive surgical margins. No conventional preoperative urological technique provides information to supplant haptic feedback.

Magnetic resonance (MR) imaging of the prostate with use of an endorectal coil spatially localizes prostate cancers, especially those that are of a higher volume and higher grade

Advances in Knowledge

- MR imaging information influenced the extent of surgery (nerve-sparing vs non-nerve-sparing technique) in 28 of the 104 patients (27%) who underwent robotic-assisted laparoscopic prostatectomy (RALP).
- Adding MR imaging data to the clinical information to determine the extent of surgery did not result in additional positive margins at surgery (0 of 28 patients).

(5–12). Preoperative knowledge of tumor location and pathologic stage, that is, the presence of extracapsular extension or seminal vesicle invasion, provides the robotic surgeon additional information that can be used to plan the surgical technique. The purpose of this study was to determine whether findings at preoperative endorectal coil MR imaging influence the decision to preserve neurovascular bundles and the extent of surgical margins in RALP.

Materials and Methods

Patient Selection

The study was approved by our institutional review board and was compliant with the Health Insurance Portability and Accountability Act. The institutional review board determined that the requirement to obtain specific consent for the study was not necessary because treatment was within the standard of care (written informed consent was obtained explicitly for MR imaging and surgery, with the understanding that surgical extent would be based on the imaging

Implications for Patient Care

- Prostate MR imaging data complement clinical information to help surgeons determine whether to perform nerve-sparing or non-nerve-sparing RALP in 27% of patients.
- Some patients thought to require non-nerve-sparing surgery might safely undergo nerve-sparing surgery on the basis of MR imaging findings because this change in surgical plan does not appear to be associated with an increase in positive surgical margins.
- MR imaging can help localize the side of stage T3 disease so that only an ipsilateral neurovascular bundle may be resected; the contralateral side may safely undergo nerve-sparing resection to minimize postoperative incontinence or impotency.

findings). Between January 2004 and April 2008, we prospectively identified 105 consecutive patients who met the inclusion criterion of MR imaging of the prostate with an endorectal coil before RALP (Table 1); one patient who underwent open prostatectomy rather than RALP was excluded. Biopsy-proved adenocarcinoma of the prostate gland was diagnosed in all patients before MR imaging.

Demographics

Patient cancer grade and stage are summarized in Table 2. Not all patients underwent all components of the MR imaging prostate examination. All patients underwent T2-weighted MR imaging. In addition to T2-weighted MR imaging, 16 patients underwent MR spectroscopy, 36 patients underwent both MR spectroscopy and diffusion-weighted imaging, 12 patients underwent both diffusion-weighted imaging and dynamic contrast material-enhanced imaging, and one patient underwent diffusion-weighted imaging. Thirty-nine patients underwent all four components. The variability of MR components occurred for two reasons. First, spectroscopic imaging was not covered by all insurers; therefore, not all patients elected to pay out of pocket for spectroscopy. Second, both diffusion-weighted and dynamic

Published online before print

10.1148/radiol.11103504 **Content code:** 

Radiology 2012; 262:874–883

Abbreviations:

PSA = prostate-specific antigen
RALP = robotic-assisted laparoscopic prostatectomy

Author contributions:

Guarantors of integrity of entire study, T.D.M., D.J.A.M., S.S.R.; study concepts/study design or data acquisition or data analysis/interpretation, all authors; manuscript drafting or manuscript revision for important intellectual content, all authors; manuscript final version approval, all authors; literature research, T.D.M., D.J.A.M., M.A.T., M.G., S.S.R.; clinical studies, T.D.M., D.J.A.M., R.E.R., M.G., S.S.R.; statistical analysis, T.D.M., D.J.A.M., J.W.S.; and manuscript editing, T.D.M., D.J.A.M., R.E.R., J.W.S., M.A.T., M.G., S.S.R.

Potential conflicts of interest are listed at the end of this article.

Table 1

Patient Demographics					
Characteristic	Mean	Median	Maximum	Minimum	Standard Deviation
Age (y)	60.1	59.7	85	41	6.8
Serum PSA level (ng/dL)	6.5	5.3	43.10	1.01	4.7
Time between MR imaging and surgery (wk)	7.7	4.9	56	0	9.1
Time between biopsy and MR imaging (wk)	12.7	11.3	46	2	6.9

contrast-enhanced imaging became available at different times during the course of the study.

MR Imaging

All 104 patients underwent imaging with a 1.5-T unit with high-performance gradients (Avanto; Siemens Medical Solutions, Erlangen, Germany) by using an inflatable endorectal coil (Medrad, Indianola, Pa) insufflated with 60–90 mL of room air. All patients underwent sagittal, coronal, and axial oblique turbo spin-echo T2-weighted imaging. In 88 of the 104 patients (85%), echoplanar diffusion-weighted imaging was performed with calculation of apparent diffusion coefficients. In 51 of the 104 patients (49%), dynamic contrast-enhanced imaging was performed by using time-resolved imaging with stochastic trajectories, a k-space-sharing three-dimensional gradient-recalled echo sequence (with 0.1 mg/kg gadopentetate dimeglumine injected at 2 mL/sec with the third of 14 acquisitions; reconstructed voxel size was $0.9 \times 1.2 \times 1.5$ mm). MR spectroscopy was performed in 91 of the 104 patients (88%). An echo time of 120 msec was used for optimal citrate resonance. Data were processed online by using the Siemens postprocessing package. Imaging parameters are given in Table 3.

Image Analysis

All images were analyzed prospectively by consensus of two fellowship-trained genitourinary radiologists (S.S.R. and D.J.A.M., with 12 and 5 years of experience, respectively), who were initially blinded to clinical data. Criteria for the presence of cancer on T2-weighted

images included round, ovoid, or irregular areas of low signal intensity on T2-weighted images without corresponding high T1 signal intensity, which might indicate hemorrhage. Criteria for extracapsular extension at MR imaging that have been found to be specific in previous studies included the presence of low signal intensity in the peripheral zone of the prostate with irregular bulging or bowing of the prostate capsule at T2-weighted imaging, disruption of the low-signal-intensity periprostatic band at T2-weighted imaging, or direct involvement of the neurovascular bundle and/or obliteration of the retroprostatic angle (5,11–13). The likelihood of extracapsular extension, as a composite score based on T2- and diffusion-weighted imaging, dynamic contrast-enhanced imaging, and MR spectroscopy as available, was prospectively reported as low, intermediate, or high for each side, with intermediate and high cases combined for binary analysis because this was the consideration of the surgeon. When apparent diffusion coefficient maps, dynamic contrast-enhanced images, and MR spectroscopic images were available, these were also used to inform the degree of suspicion. Lesions were considered suspicious if at least one of the following findings was present: restricted diffusion, early or intense enhancement, washout, or elevated choline-to-citrate ratio. All MR spectroscopic data were obtained and analyzed under the supervision of a physicist with more than 15 years of experience in endorectal MR imaging (M.A.T.). Voxels were considered sufficient for analysis if one metabolite had a signal-to-noise ratio of at least 4:1.

Voxels were considered positive for tumor when the ratio of choline and creatine to citrate was at least 1:3 on at least four contiguous voxels.

Imaging results were evaluated, and disease stage was assigned according to the American Joint Committee on Cancer Staging of Prostate Cancer (TNM system); thus, neurovascular bundle involvement was not separately recorded.

Robotic Prostatectomy Algorithm

RALP was performed by one surgeon (R.E.R., with more than 6 years of experience with this technique) with use of a Da Vinci robot (Intuitive Surgical, Sunnyvale, Calif). The surgeon initially formulated a resection plan (bilateral nerve-sparing surgery, bilateral non-nerve-sparing surgery, or a combination of unilateral non-nerve-sparing and nerve-sparing surgery) blinded to MR results on the basis of a composite of the following clinical variables: results of digital rectal examination, results of sextant prostate biopsy (including Gleason score, number of positive core specimens, percentage of positive core specimens, and tumor length), and serum prostate-specific antigen (PSA) level. The resection plan was reevaluated after review of the MR imaging results. The nerve-sparing technique was reserved for patients without intermediate or high probability of extracapsular extension or neurovascular bundle involvement. The surgical technique was documented in the surgery report.

Surgical-Pathologic Examination

The prostate was serially sectioned (not whole mount) from base to apex into different levels (depending on the size of the prostate) for histologic analysis and labeled as right or left and anterior or posterior apex, midgland, and base. The right and left seminal vesicle and vas deferens were also analyzed separately. Slides were reviewed by experienced genitourinary pathologists who were not aware of imaging findings per standard clinical protocol. All reports were reviewed to determine the presence of extracapsular extension or seminal vesicle invasion and to compare

Table 2

Biopsy and Surgical Specimen Gleason Score with Surgery Type

Biopsy Gleason Score	No. of Patients	Surgical Specimen Gleason Score				Nerve-Sparing Surgery	
		3 + 3 = 6	3 + 4 = 7	4 + 3 = 7	4 + 4 = 8	Initial Plan	Actual Surgery
3 + 3 = 6	60 (58)	27	29	3	1	47	48
3 + 4 = 7	30 (29)	5	18	7	0	18	20
4 + 3 = 7	10 (10)	1	4	3	2	4	6
4 + 4 = 8	4 (4)	2	1	1	0	2	2
Total	104	35 (34)	52 (50)	14 (13)	3 (3)	71 (68)	76 (73)

Note.—Data are numbers of patients, with percentages in parentheses. Gleason score ranking was performed with the following algorithm: 3 + 3 = 6 (rank 1), 3 + 4 = 7 (rank 2), 4 + 3 = 7 (rank 3), and 4 + 4 = 8 (rank 4).

Table 3

Imaging Parameters

Imaging Technique*	No. of Patients	Orientation	TR/TE†	Matrix	Field of View	Section Thickness and Gap (mm)	Other Parameters
TSE T2 weighted	104	Three plane	3800/101	205 × 256	14 cm	3 and 0	Echo train length, 32; two signals acquired
DW imaging	88	Axial	1600/75	256 × 154	35 × 26 cm	5 and 1.7	<i>b</i> = 0, 150, 400 msec
DCE imaging	51	Axial	6.8/2.86	320 × 225	30 × 28 cm	1.5 and 0	25° flip angle; 14 sequences, each 15 sec
MR spectroscopy‡	91	Three-dimensional chemical shift imaging	700/120	12 × 12 × 12	8 cm ³	NA§	1300-Hz bandwidth; six signals acquired

* DCE = dynamic contrast enhanced, DW = diffusion weighted, TSE = turbo spin echo.

† TR/TE = repetition time msec/echo time msec.

‡ MR spectroscopy included water and fat suppression. Imaging time was approximately 12 minutes, with 2 minutes dedicated to manual shimming. A point-resolved spectroscopy sequence was used to acquire proton MR spectra from a volume of interest of 55 × 30 × 40 mm³. Outer volume lipid suppression was achieved with eight 3-cm-thick saturation pulses around the volume of interest by using two 12.6-msec dual-frequency selective Mescher-Garwood (or MEGA) pulses with crusher gradients.

§ NA = not applicable.

staging at pathologic examination and imaging.

Statistical Analysis

The following variables were recorded for each patient: age, serum PSA level, original surgical plan, final surgical plan, biopsy Gleason score, final pathologic Gleason score, weeks between biopsy and MR imaging, weeks between MR imaging and surgery, and components of MR imaging (spectroscopy, diffusion-weighted imaging, and dynamic contrast-enhanced imaging). Binary variables were assigned separately for the right and left side for each patient for both MR imaging stage and surgical stage (T2 vs T3) and for surgical margins. The type

of surgery performed (nerve-sparing vs non-nerve-sparing surgery) and whether the planned surgery changed on the basis of imaging findings was also assigned a binary variable separately for the right and left side. The Gleason score, which was determined at both biopsy and surgery, was analyzed separately and converted to ranked categories (see footnote in Table 2). Serum PSA level and patient age were analyzed as continuous variables. The time between biopsy and MR imaging and between MR imaging and surgery was also analyzed as a continuous variable. Binary variables underwent multivariate logistic regression analysis. Continuous and ranked variables underwent Pearson

product moment and nonparametric Spearman rank correlation analysis with use of software (SPSS PASW 17; SPSS, Chicago, Ill). Although the sample size appeared large enough for Pearson product moment, because we initially planned on evaluating the Spearman rank correlation, this analysis is also presented. *P* ≤ .05 was considered indicative of a statistically significant difference.

Results

Effect on Surgery and Surgical Margins

The initial planned surgical technique was changed following review of the MR imaging data on at least one side

Figure 1

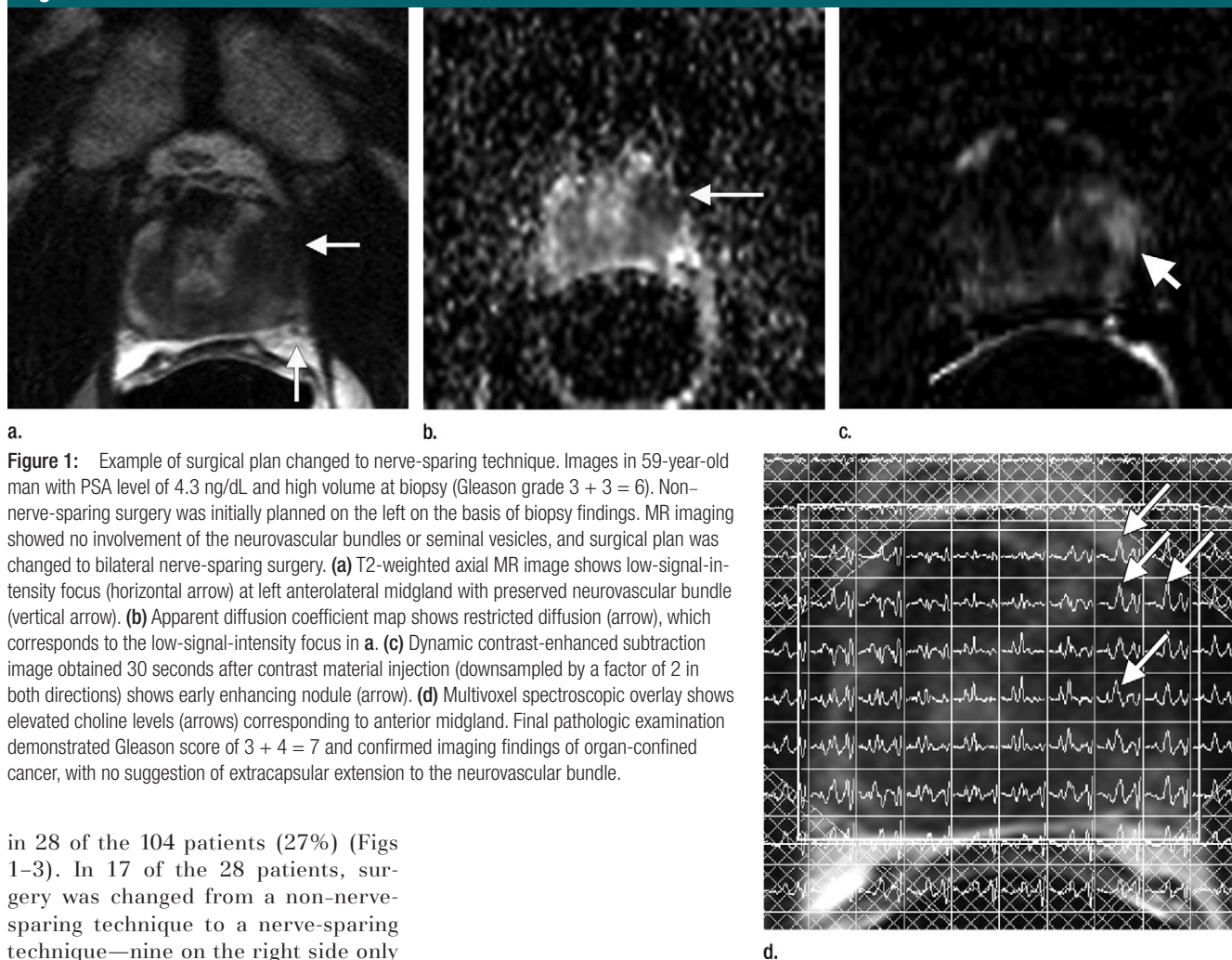


Figure 1: Example of surgical plan changed to nerve-sparing technique. Images in 59-year-old man with PSA level of 4.3 ng/dL and high volume at biopsy (Gleason grade 3 + 3 = 6). Non-nerve-sparing surgery was initially planned on the left on the basis of biopsy findings. MR imaging showed no involvement of the neurovascular bundles or seminal vesicles, and surgical plan was changed to bilateral nerve-sparing surgery. **(a)** T2-weighted axial MR image shows low-signal-intensity focus (horizontal arrow) at left anterolateral midgland with preserved neurovascular bundle (vertical arrow). **(b)** Apparent diffusion coefficient map shows restricted diffusion (arrow), which corresponds to the low-signal-intensity focus in **a**. **(c)** Dynamic contrast-enhanced subtraction image obtained 30 seconds after contrast material injection (downsampled by a factor of 2 in both directions) shows early enhancing nodule (arrow). **(d)** Multivoxel spectroscopic overlay shows elevated choline levels (arrows) corresponding to anterior midgland. Final pathologic examination demonstrated Gleason score of 3 + 4 = 7 and confirmed imaging findings of organ-confined cancer, with no suggestion of extracapsular extension to the neurovascular bundle.

in 28 of the 104 patients (27%) (Figs 1–3). In 17 of the 28 patients, surgery was changed from a non-nerve-sparing technique to a nerve-sparing technique—nine on the right side only and seven on the left side only. In one patient, surgery was changed from a non-nerve-sparing to a nerve-sparing technique on the right but from a nerve-sparing to a non-nerve-sparing technique on the left. In 11 of the 28 patients, surgery was changed from a nerve-sparing to a non-nerve-sparing technique—six on the right side only, four on the left side only, and one bilaterally.

Surgical margins were positive in five patients on the right side only, in one patient on the left side only, and in one patient bilaterally. In two of these cases, the surgical plan was changed—but on the side opposite of the positive margin. In no case of positive margins was the surgery changed to nerve-sparing surgery on the side

of the positive margins. In four additional cases, margins were only focally positive at the apex, which is considered a negative margin because this has not been shown to confer a worse prognosis than organ-confined disease (14) and is managed by urologists as a negative margin.

Positive margins coincided with pathologic stage T3 (pT3) disease bilaterally in the case of bilateral positive margins and ipsilaterally in one case of left-sided positive margins; all other cases of positive margins occurred in stage pT2 disease, where the surgical margin was inside the prostate capsule and tumor was within 1 mm of the margin. Non-nerve-sparing surgery was

performed bilaterally in the one patient with bilateral positive margins and ipsilaterally in one patient with positive margins on the right side; in all other cases of positive margins, nerve-sparing surgery was performed on the positive side.

Diffusion-weighted imaging was performed in all patients with positive margins and dynamic contrast-enhanced imaging was performed in five. MR spectroscopy was performed in all patients except the two with stage pT3 disease.

Radiologic-Pathologic Correlation

In all but one patient, tumors were either posterior or both anterior and posterior.

Figure 2

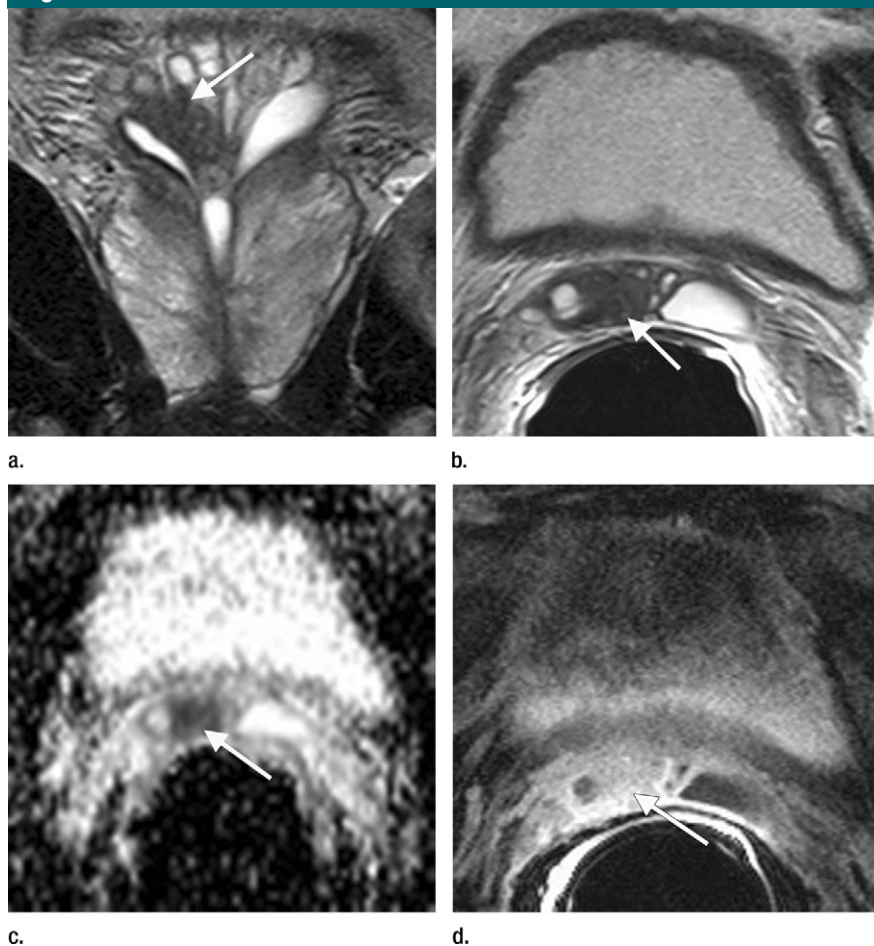


Figure 2: Example of surgical plan changed to non-nerve-sparing technique. Images in 53-year-old man with PSA level of 14 ng/dL and biopsy Gleason score of 3 + 3 = 6 in two of six core specimens on the right. On the basis of these findings, bilateral nerve-sparing surgery was initially planned. After MR imaging, however, surgical plan was changed to a non-nerve-sparing technique on the right. **(a)** Coronal and **(b)** axial T2-weighted images show a low-signal-intensity mass (arrow) extending into the right seminal vesicle. **(c)** Apparent diffusion coefficient map shows restricted diffusion (arrow), corresponding to the low-signal-intensity focus on T2-weighted images. **(d)** Contrast-enhanced fat-saturated T1-weighted gradient-echo image shows enhancing nodule (arrow), corresponding to the area of low signal intensity on T2-weighted images. Final pathologic analysis demonstrated Gleason score of 4 + 3 = 7 and confirmed imaging findings of right seminal vesicle invasion.

The one patient with anterior cancer had stage T2 disease at pathologic examination and MR imaging. Whether these tumors were central, peripheral, or both was not recorded reliably by the pathologist; therefore, this was not included in the analysis. Of eight patients with stage pT3 disease, disease was on the left in four patients, on the right in two, and bilateral in two. The computed sensitivity, specificity, and positive and negative predictive values for predicting stage T3

disease according to side are 50% (five of 10 cases), 97.5% (193 of 198 cases), 50% (five of 10 cases), and 97.5% (193 of 198 cases), respectively (Table 4). In 11 of the 104 patients, the stage determined with imaging was discordant with that determined at pathologic examination. In one patient (who underwent both diffusion-weighted and dynamic contrast-enhanced imaging), disease was staged as T3b at MR imaging but was T3a at pathologic examination. Of the remaining

10 patients, one patient (who underwent MR spectroscopy but not dynamic contrast-enhanced or diffusion-weighted imaging) was classified with stage T3a disease on the right and stage T2 disease on the left at MR imaging but was stage pT3a bilaterally, four patients (one who underwent MR spectroscopy alone, two who underwent both diffusion-weighted and dynamic contrast-enhanced imaging, and one who underwent all three components) were classified with stage T2 disease at MR imaging and stage pT3 disease at pathologic examination, and the last three patients (one who underwent diffusion-weighted imaging and MR spectroscopy and two who underwent all three components) were classified with stage T3 disease at MR imaging but stage pT2 disease at pathologic examination. Of the mismatches, two patients had positive margins—one patient was understaged as having stage T2 disease with microscopic extracapsular extension at MR imaging (diffusion-weighted and dynamic contrast-enhanced imaging) and one was determined to have stage T2 disease on the side of the positive margin at both MR imaging and pathologic examination (discordant contralaterally). It should be noted that “possible microscopic extracapsular extension” at MR imaging was recorded for 47 patients. Finally, of 173 sides in which the original plan was for nerve-sparing surgery, 168 (97.1%) were classified as stage T2 at MR imaging. Of these 168 sides, 163 (97%) were pathologically proved to be stage pT2. The breakdown of patients according to surgical plan and surgical margin status is provided in Figure 4.

Statistical Analysis

Analysis of imaging stage according to side found a significant association with surgical stage and a change in surgery bilaterally but a significant association with stage pT3 disease and positive margins on the left only (Table 5). Logistic regression analysis of positive margins showed no association with change in surgery and a significant relationship with imaging and surgical stage on the left but not on the right. No association was found between absence of any of the

Figure 3

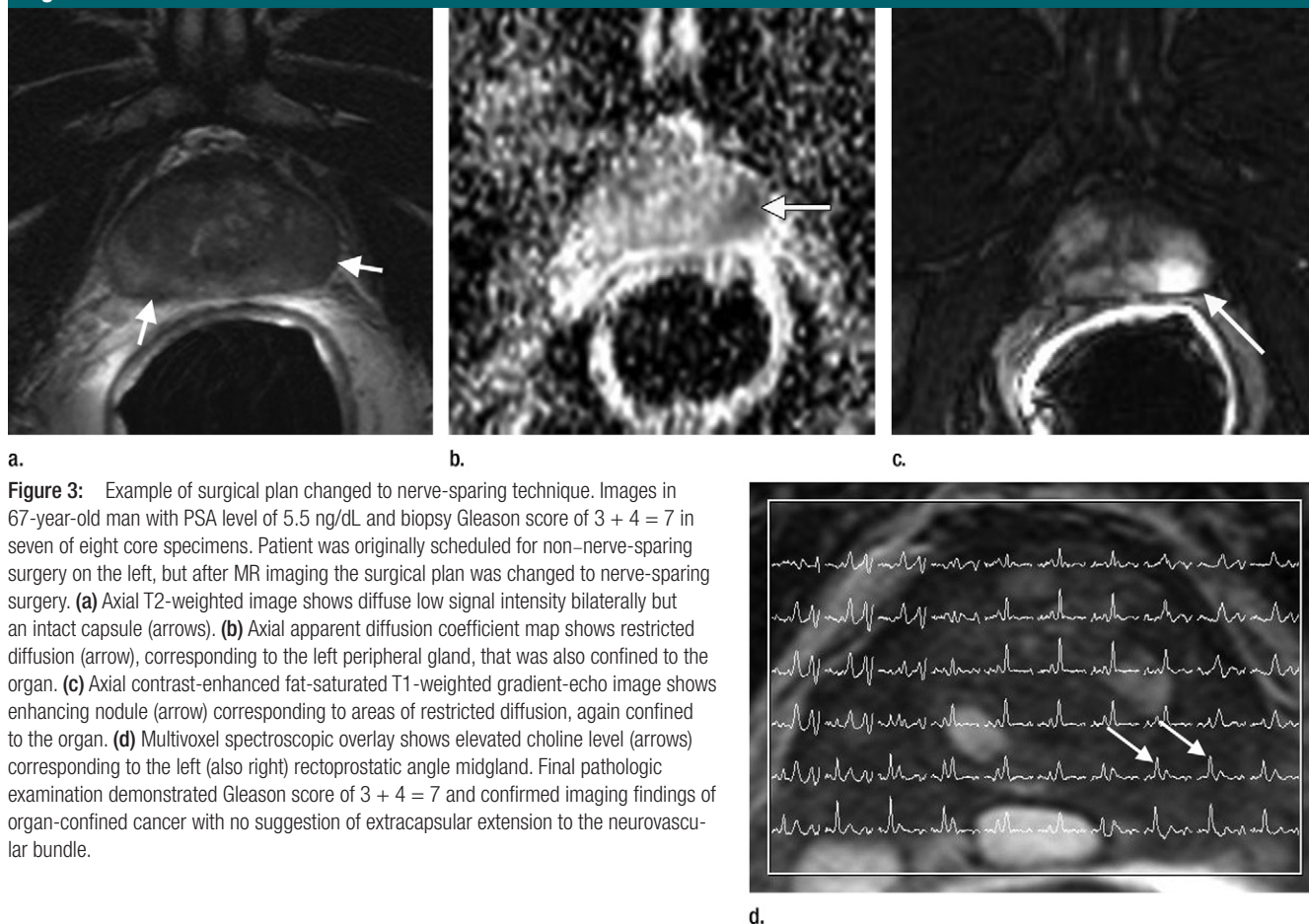


Figure 3: Example of surgical plan changed to nerve-sparing technique. Images in 67-year-old man with PSA level of 5.5 ng/dL and biopsy Gleason score of 3 + 4 = 7 in seven of eight core specimens. Patient was originally scheduled for non-nerve-sparing surgery on the left, but after MR imaging the surgical plan was changed to nerve-sparing surgery. **(a)** Axial T2-weighted image shows diffuse low signal intensity bilaterally but an intact capsule (arrows). **(b)** Axial apparent diffusion coefficient map shows restricted diffusion (arrow), corresponding to the left peripheral gland, that was also confined to the organ. **(c)** Axial contrast-enhanced fat-saturated T1-weighted gradient-echo image shows enhancing nodule (arrow) corresponding to areas of restricted diffusion, again confined to the organ. **(d)** Multivoxel spectroscopic overlay shows elevated choline level (arrows) corresponding to the left (also right) rectoprostatic angle midgland. Final pathologic examination demonstrated Gleason score of 3 + 4 = 7 and confirmed imaging findings of organ-confined cancer with no suggestion of extracapsular extension to the neurovascular bundle.

components of MR imaging (diffusion-weighted imaging, dynamic contrast-enhanced imaging, or MR spectroscopy) and margins, grade, stage (at imaging or pathologic examination), surgery type, or change in surgical plan owing to imaging findings.

A significant Pearson correlation was found between surgical grade and both serum PSA level and stage pT3 disease and between biopsy grade and serum PSA level but not stage pT3 disease, and neither had a significant correlation with age or change in surgery (Table 6). A significant correlation was also found between age and change in surgery. At Spearman rank coefficient analysis, we found a significant correlation between surgical grade and PSA level and stage pT3 disease as well as change in surgery and between biopsy grade and PSA level but none of the other parameters. Again,

a significant correlation was found between age and change in surgery.

Discussion

Approximately 40% of patients with localized prostate cancer choose some form of surgical resection for treatment (15). In 2008, approximately 60 000 patients opted to undergo RALP rather than conventional open prostatectomy (16). In any surgical approach, surgeons must balance the desire to achieve a cancer-free resection margin with the need to minimize postoperative morbidity, which with prostate cancer surgery includes incontinence, impotence, and erectile dysfunction. The neurovascular bundles, which mediate erectile function and continence (17), lay posterolateral to the prostatic capsule and adjacent to the peripheral zone, where

70% of cancers arise. In open radical prostatectomy, surgeons typically identify and spare both neurovascular bundles to preserve patient potency (18). However, a surgeon who believes that an area beyond the capsule is suspicious for cancer can widely resect the neurovascular bundle and surrounding tissue to achieve negative surgical margins. By resecting the neurovascular bundle, the risk of postoperative impotence increases substantially (19).

During RALP, surgeons lack the tactile feedback they rely on during open surgery to determine the extent of malignant involvement and resection, potentially affecting surgical outcome. As in open radical prostatectomy, surgeons performing RALP routinely dissect the neurovascular bundles off the prostatic capsule and spare the nerves—but without haptic feedback. Unlike clinical

Table 4

Imaging versus Pathologic Stage

Parameter*	Pathologic Stage	
	T2	T3
MR imaging stage		
T2	193	5
T3	5	5
Sensitivity (%)	50	...
Specificity (%)	...	97.5
PPV (%)	50	...
NPV (%)	...	97.5

* NPV = negative predictive value, PPV = positive predictive value.

variables (PSA level, findings from digital rectal examination), results from prostate MR imaging are spatially localized and allow surgeons to individually sculpt the extent of surgical resection (20). Prostate MR imaging data map an individual cancer's relationship to the capsule and neurovascular bundles, thus assisting in the determination of performing nerve-sparing versus non-nerve-sparing surgery. A priori knowledge of extracapsular extension would allow the surgeon to plan non-nerve-sparing resection of the neurovascular bundle on the involved side (21). Conversely, sparing the neurovascular bundles when extracapsular extension is present increases the probability of a positive surgical margin, the need for postoperative radiation therapy, and local cancer recurrence (22).

In patients undergoing open radical prostatectomy, MR imaging has been shown to improve the accuracy of the surgeon's decision to resect or preserve the neurovascular bundles (20). Our study differs from this landmark study in several ways. First, our study could be viewed by some as being more consistent with true clinical practice because the surgical plan was informed by the report and online images but rarely by direct radiologist consultation. In addition, not all patients underwent MR spectroscopy. The main reason why MR spectroscopy was not performed in all patients is because it is not covered by most insurance carriers and not all patients

Figure 4

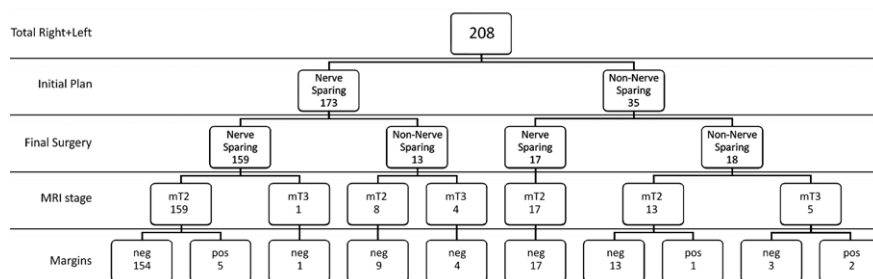


Figure 4: Diagram shows the relative number of patients stratified according to surgery, imaging findings, and surgical margins. *neg* = Negative, *pos* = positive.

Table 5

Results of Multivariate Logistic Regression Analysis

Parameter	Right Side	Left Side
MR imaging stage T3		
Stage pT3 disease	44.785 (<.001)	11.188 (.001)
Change in surgery	26.881 (<.001)	19.732 (<.001)
Positive margins	1.957 (.162)	9.000 (.003)
Positive margins		
Stage pT3 disease	2.830 (.093)	15.992 (<.001)
Change in surgery	1.344 (.342)	2.337 (.126)

Note.—Numbers in parentheses are P values.

can pay for the additional cost. Another difference between studies is that our scoring of stage T3 disease at MR imaging and the surgical plan was binary, not quinary. Although this precludes receiver operating characteristic analysis, the surgeon's decision to spare or resect neurovascular bundles was, in the context of this analysis, binary; therefore, it was requested that our assessment of stage at imaging reflect this. In addition, all of the images in our study were read by the same two radiologists to reduce the likelihood of interobserver bias; in the previous study, all images were read by one of two radiologists. Last, an important point is that we looked at how MR imaging changed the surgical plan and the final pathologic diagnosis, not just the presence of positive surgical margins as in the previous study. The correlation of imaging and pathologic findings was not our primary end point; rather, we wanted to evaluate the impact of MR imaging

data on the extent of surgical resection bilaterally. This last aspect is the most important because the tactile response of the surgeon using robotic technology is limited, increasing the reliance on imaging for determining stage. This informs the selection of patients because this technique is optimized for preservation of neurovascular bundles and is therefore of less value in gross T3 disease (16). In the previous study (20), all patients underwent open prostatectomy and all underwent identical imaging without diffusion-weighted or dynamic contrast-enhanced pulse sequences. Analysis in this previous study used histopathologic correlation of neurovascular bundle invasion as a primary end point for modeling risk stratification rather than analyzing the effect on surgical technique and margins. In addition, the surgical plan was altered in 39% of the neurovascular bundles in that study, which is higher than the percentage we found. This may

Table 6

Pearson Product Moment and Spearman Rank Correlation Coefficients

Parameter	Change in Surgery	Surgical Grade	Biopsy Grade	Stage T3	PSA Level
Pearson analysis					
Age	0.263 (.007)	0.078 (.429)	0.007 (.941)	0.074 (.453)	0.037 (.712)
PSA level	0.007 (.941)	0.295 (.003)	0.217 (.028)	0.141 (.156)	...
Stage T3 disease	0.013 (.900)	0.247 (.011)	0.143 (.147)
Biopsy grade	0.141 (.153)
Surgical grade	0.174 (.077)
Spearman analysis					
Age	0.234 (.017)	0.008 (.937)	0.012 (.904)	0.073 (.459)	0.056 (.577)
PSA level	0.029 (.772)	0.334 (.001)	0.213 (.031)	0.234 (.018)	...
Stage T3 disease	0.013 (.900)	0.222 (.023)	0.130 (.187)
Biopsy grade	0.121 (.222)
Surgical grade	0.199 (.043)

Note.—Numbers in parentheses are *P* values.

be due in part to patient selection and the emphasis on nerve-sparing technique placed on robotic-assisted surgery. Of 173 sides in which the original plan was for nerve-sparing surgery, 168 (97.1%) were stage T2 at MR imaging. Of these 168 sides, 163 (97%) were proved to be stage pT2 at pathologic examination.

In 28 of our 104 patients (27%), the surgical plan was changed because of information obtained only at prostate MR imaging; 17 of those 28 patients (61%) underwent nerve-sparing surgery. On the basis of the results of preoperative MR imaging and MR spectroscopy, patients were able to undergo a less morbid nerve-sparing surgery without compromising oncologic outcome. Although the overall rate of positive surgical margins was 6.7% (seven of 104 patients), 86% (six of seven patients) of these patients had undergone a more aggressive non-nerve-sparing technique with concordant MR findings on the affected side. In four additional patients, positive margins were only focally positive at the apex; this has not been shown to confer a worse prognosis than organ-confined disease (14).

The specificity of prostate MR imaging in the differentiation of T2 disease from T3 disease was 97.5%. This suggests that, in our patient population, if a patient's prostate MR image shows T2 disease, a nerve-sparing

technique can be used with a high degree of safety and without compromising oncologic outcome. Our sensitivity and specificity were higher than that reported in a recent retrospective analysis of endorectal coil MR imaging by Brajtford et al (23) (50% and 97.5% vs 43% and 73%, respectively). However, Bloch et al (24) showed a similar specificity of 95%.

Our study had several limitations. First, our final outcome "standard of reference" was positive surgical margins, not clinical outcome. Follow-up studies looking specifically at these variables are required to determine how the refinement of surgical technique guided by MR imaging findings affects patient continence and/or potency and cancer recurrence rates. Second, the final pathology reference was step-section histologic examination and not whole-mount histologic examination because this was not performed at our institution during this time. Third, our results represent one surgeon's experience with a consecutive, nonselected patient population and may not be representative of the experience at other centers. Fourth, our studies were read in consensus and therefore do not reflect clinical practice. Also, most clinical and research studies are read by one of a core group of radiologists. Fifth, because of our study design (provide the highest level of imaging

for optimal patient care, such that all patients underwent diffusion-weighted and dynamic contrast-enhanced imaging but only once available), we could not control for protocol. Finally, the protocol of the MR examinations varied, which precluded evaluation of individual components of MR imaging. Despite these limitations, our comparison of MR imaging to the standard of reference of histopathologic examination yielded excellent results. Possibly the most surprising finding was that not only were no cases of positive margins found on the side where MR imaging resulted in a change to the surgical plan, but in only one of seven cases where imaging found stage T3 disease was the surgical plan changed. This may suggest that imaging did not add to the decision because non-nerve-sparing surgery was already planned in six of these cases. Overall, however, imaging resulted in a change to the surgical plan in 28 of the 104 patients (27%), with most surgeries changed to a nerve-sparing technique; in addition, there were no positive margins on the side where the surgical plan was changed to a nerve-sparing technique, potentially decreasing the chance of postsurgical morbidity.

To our knowledge, this is the first report demonstrating the value of MR imaging in planning RALP. On the basis of our initial experience, prostate MR

imaging may be useful for helping surgeons plan the extent and side of nerve sparing during RALP.

Disclosures of Potential Conflicts of Interest:

T.D.M. No potential conflicts of interest to disclose. **D.J.A.M.** Financial activities related to the present article: institution received a grant from Siemens Medical Systems. Financial activities not related to the present article: is a consultant for MedQIA. Other relationships: none to disclose. **R.E.R.** No potential conflicts of interest to disclose. **J.W.S.** No potential conflicts of interest to disclose. **M.A.T.** Financial activities related to the present article: received a grant from Siemens Medical Systems; institution received a grant from Siemens Medical Systems. Financial activities not related to the present article: none to disclose. Other relationships: none to disclose. **R.N.** Financial activities related to the present article: received a grant from Siemens Medical Systems; institution received a grant from Siemens Medical Systems. Financial activities not related to the present article: none to disclose. Other relationships: none to disclose. **M.G.** No potential conflicts of interest to disclose. **S.S.R.** No potential conflicts of interest to disclose.

References

- Jemal A, Siegel R, Ward E, et al. Cancer statistics, 2008. *CA Cancer J Clin* 2008;58(2):71–96.
- Walsh PC, Lepor H, Eggleston JC. Radical prostatectomy with preservation of sexual function: anatomical and pathological considerations. *Prostate* 1983;4(5):473–485.
- Box GN, Ahlering TE. Robotic radical prostatectomy: long-term outcomes. *Curr Opin Urol* 2008;18(2):173–179.
- Rassweiler J, Frede T, Seemann O, Stock C, Sentker L. Telesurgical laparoscopic radical prostatectomy: initial experience. *Eur Urol* 2001;40(1):75–83.
- Chandra RV, Heinze S, Dowling R, Shadbolt C, Costello A, Pedersen J. Endorectal magnetic resonance imaging staging of prostate cancer. *ANZ J Surg* 2007;77(10):860–865.
- desouza NM, Reinsberg SA, Scurr ED, Brewster JM, Payne GS. Magnetic resonance imaging in prostate cancer: the value of apparent diffusion coefficients for identifying malignant nodules. *Br J Radiol* 2007;80(950):90–95.
- Kozlowski P, Chang SD, Jones EC, Berean KW, Chen H, Goldenberg SL. Combined diffusion-weighted and dynamic contrast-enhanced MRI for prostate cancer diagnosis: correlation with biopsy and histopathology. *J Magn Reson Imaging* 2006;24(1):108–113.
- Scheidler J, Hricak H, Vigneron DB, et al. Prostate cancer: localization with three-dimensional proton MR spectroscopic imaging—clinicopathologic study. *Radiology* 1999;213(2):473–480.
- Turkbey B, Pinto PA, Mani H, et al. Prostate cancer: value of multiparametric MR imaging at 3 T for detection—histopathologic correlation. *Radiology* 2010;255(1):89–99.
- Wang L, Hricak H, Kattan MW, Chen HN, Scardino PT, Kuroiwa K. Prediction of organ-confined prostate cancer: incremental value of MR imaging and MR spectroscopic imaging to staging nomograms. *Radiology* 2006;238(2):597–603.
- Yu KK, Hricak H, Alagappan R, Chernoff DM, Bacchetti P, Zaloudek CJ. Detection of extracapsular extension of prostate carcinoma with endorectal and phased-array coil MR imaging: multivariate feature analysis. *Radiology* 1997;202(3):697–702.
- Yu KK, Scheidler J, Hricak H, et al. Prostate cancer: prediction of extracapsular extension with endorectal MR imaging and three-dimensional proton MR spectroscopic imaging. *Radiology* 1999;213(2):481–488.
- Outwater EK, Petersen RO, Siegelman ES, Gomella LG, Chernesky CE, Mitchell DG. Prostate carcinoma: assessment of diagnostic criteria for capsular penetration on endorectal coil MR images. *Radiology* 1994;193(2):333–339.
- Fesseha T, Sakr W, Grignon D, Banerjee M, Wood DP Jr, Pontes JE. Prognostic implications of a positive apical margin in radical prostatectomy specimens. *J Urol* 1997;158(6):2176–2179.
- Bhatnagar V, Kaplan RM. Treatment options for prostate cancer: evaluating the evidence. *Am Fam Physician* 2005;71(10):1915–1922.
- Pruthi RS, Wallen EM. Current status of robotic prostatectomy: promises fulfilled. *J Urol* 2009;181(6):2420–2421.
- Walsh PC. Radical retropubic prostatectomy with reduced morbidity: an anatomic approach. *NCI Monogr* 1988;(7):133–137.
- Gralnek D, Wessells H, Cui H, Dalkin BL. Differences in sexual function and quality of life after nerve sparing and nonnerve sparing radical retropubic prostatectomy. *J Urol* 2000;163(4):1166–1169; discussion 1169–1170.
- Kundu SD, Roehl KA, Eggener SE, Antenor JA, Han M, Catalona WJ. Potency, continence and complications in 3,477 consecutive radical retropubic prostatectomies. *J Urol* 2004;172(6 Pt 1):2227–2231.
- Hricak H, Wang L, Wei DC, et al. The role of preoperative endorectal magnetic resonance imaging in the decision regarding whether to preserve or resect neurovascular bundles during radical retropubic prostatectomy. *Cancer* 2004;100(12):2655–2663.
- Poulakis V, de Vries R, Dillenburg W, Altmanberger HM, Becht E. Laparoscopic radical prostatectomy: impact of modified apical and posterolateral dissection in reduction of positive surgical margins in patients with clinical stage T2 prostate cancer and high risk of extracapsular extension. *J Endourol* 2006;20(5):332–339.
- Rosen MA, Goldstone L, Lapin S, Wheeler T, Scardino PT. Frequency and location of extracapsular extension and positive surgical margins in radical prostatectomy specimens. *J Urol* 1992;148(2 Pt 1):331–337.
- Brajtford J, Lavery H, Nabizada-Pace F, Senaratne P, Samadi D. Endorectal magnetic resonance imaging has limited clinical ability to preoperatively predict pT3 prostate cancer. *BJU Int* 2011;107(9):1419–1424.
- Bloch BN, Furman-Haran E, Helbich TH, et al. Prostate cancer: accurate determination of extracapsular extension with high-spatial-resolution dynamic contrast-enhanced and T2-weighted MR imaging—initial results. *Radiology* 2007;245(1):176–185.

Application of Compressed Sensing to Multidimensional Spectroscopic Imaging in Human Prostate

Jon K. Furuyama, Neil E. Wilson, Brian L. Burns, Rajakumar Nagarajan, Daniel J. Margolis, and M. Albert Thomas*

The application of compressed sensing is demonstrated in a recently implemented four-dimensional echo-planar based J-resolved spectroscopic imaging sequence combining two spatial and two spectral dimensions. The echo-planar readout simultaneously acquires one spectral and one spatial dimension. Therefore, the compressed sensing undersampling is performed along the indirectly acquired spatial and spectral dimensions, and the reconstruction is performed using the split Bregman algorithm, an efficient TV-minimization solver. The four-dimensional echo-planar-based J-resolved spectroscopic imaging data acquired in a prostate phantom containing metabolites at physiological concentrations are accurately reconstructed with as little as 20% of the original data. Experimental data acquired in six healthy prostates using the external body matrix “receive” coil on a 3T magnetic resonance imaging scanner are reconstructed with acquisitions using only 25% of the Nyquist–Shannon required amount of data, indicating the potential for a 4-fold acceleration factor in vivo, bringing the required scan time for multidimensional magnetic resonance spectroscopic imaging within clinical feasibility. Magn Reson Med 67:1499–1505, 2012. © 2012 Wiley Periodicals, Inc.

Key words: Compressed sensing; prostate; magnetic resonance; citrate; echo-planar J-resolved spectroscopic imaging

Magnetic resonance spectroscopy and magnetic resonance spectroscopic imaging have evolved as powerful research tools for their ability to study the underlying biochemistry of tissue (1) and can greatly complement standard magnetic resonance imaging (MRI). One of the major drawbacks of one-dimensional (1D) spectroscopy is the inherent overcrowding of spectra due to overlapping peaks. This limitation can be alleviated with the addition of more spectral dimensions by which resonances can be spread apart, increasing the spectral dispersion (2). Different two-dimensional (2D) spectroscopic techniques have been successfully used in vivo such as J-resolved spectroscopy (3) and localized correlated spectroscopy (4). However, these were originally limited to single voxel acquisitions. To increase the spatial coverage, the localized correlated

spectroscopy and J-resolved spectroscopy sequences were recently modified with an echo-planar spectroscopic imaging (EPSI) (5–7) readout to yield 2D spectra from multiple voxels in a single experiment, called echo-planar correlated spectroscopic imaging (8) and echo-planar J-resolved spectroscopic imaging (EP-JRESI) (9), respectively. Despite the rapid acquisition of EPSI, such four-dimensional (4D) scans still require a considerable amount of scan time (~20–40 mins/average depending on the desired spatial/spectral resolution), severely limiting clinical applicability.

In recent years, the field of compressed sensing (CS) has garnered much interest in the imaging community for its ability to reconstruct images from datasets whose sampling does not meet the Nyquist–Shannon criterion (10,11). CS operates under the assumption that the fully sampled data is sparse within some transform domain. The CS reconstruction attempts to enforce this assumption in that particular transform domain, while maintaining fidelity with the acquired measurements. Since the application of CS in MRI was demonstrated (12,13), there has been a trove of proposed applications for imaging studies as well as high resolution nuclear magnetic resonance, many of which hold the potential to reduce scan times by a factor of 2–8 times (14–18).

Despite the many potential applications in standard MRI, there have not been many proposed implementations for use in magnetic resonance spectroscopic imaging (19). Part of the reason is that while CS can provide acceleration factors ranging from 2 to 8 times in standard chemical shift imaging with multiple phase encoding directions, the acceleration factor of using an EPSI readout is on the order of 16–32. The challenge is thus to further accelerate EPSI with CS. Since EPSI simultaneously reads out one spatial and one spectral dimension, there remains only one dimension that can be undersampled in a 2D spatial acquisition. However, it has been previously discussed that CS can perform better when the undersampling is spread across multiple dimensions (20). Hu et al. employed pseudo-random phase-encoding blips during the EPSI readout to create nonuniform sampling along the spatial as well as spectral dimensions for use in hyperpolarized ^{13}C spectroscopic imaging (19).

In the EP-JRESI sequence, the EPSI readout simultaneously acquires one spatially encoded dimension (k_x) and one temporal dimension (t_2), leaving the remaining spatial and spectral dimensions (k_y and t_1 , respectively) to be incrementally collected. We propose the use of nonuniform undersampling (NUS) in the remaining $k_y t_1$ plane, using CS to reconstruct the equivalent missing data to a fully sampled 4D EP-JRESI acquisition. Despite the mixing

Department of Radiological Sciences, University of California, Los Angeles, California, USA

Grant sponsor: IDEA (US Army Department of Defense); Grant sponsor: Prostate Cancer Research Program (PCRP); Grant number: W81XWH-11-1-0248

*Correspondence to: M. Albert Thomas, Ph.D., Department of Radiological Sciences, University of California, Los Angeles, CA 90095. E-mail: AThomas@mednet.ucla.edu

Received 23 November 2011; revised 27 February 2012; accepted 28 February 2012.

DOI 10.1002/mrm.24265

Published online 13 April 2012 in Wiley Online Library (wileyonlinelibrary.com).

of spatial and spectral dimensions in the reconstruction, the sparsity requirement for reconstruction is shown to still be satisfied, as required by CS. Since the $k_y t_1$ plane is incrementally acquired, NUS can be trivially applied to the sequence without pseudo-random gradient blips.

Using fully sampled prostate phantom datasets, the NUS can be simulated and the data can be reconstructed using publicly available ℓ_1 -norm minimization algorithms. We show that the CS reconstruction performs favorably with as little as 20–25% of the original data, implying an acceleration factor of 4–5 times and scan times less than 4–5 mins for the NUS 4D EP-JRESI sequence. Nonuniformly undersampled data were collected in the prostate of healthy volunteers amounting to 25% of the sampling required by the Nyquist–Shannon criterion. The reconstructed NUS data shows good spatial and spectral quality in the undersampled dimensions, comparable to the fully sampled reconstruction.

THEORY

In order for CS to be successfully applied, the following criteria must be satisfied. First, the data must have a sparse representation: namely, there must exist some transform domain in which the data has many coefficients that are zero or nearly zero. Second, the NUS must be such that it produces incoherent aliasing artifacts within the transform domain, which is easily obtained by sampling the dataset at random. With these conditions, the fully sampled dataset can be recovered using nonlinear reconstruction algorithms that attempt to enforce the sparsity while simultaneously maintaining the fidelity of the original measurements to within the noise. CS solves the constrained optimization problem (12)

$$\min_m \|\Psi m\|_1 \quad \text{s.t.} \|\mathcal{F}_u m - y\|_2^2 < \epsilon^2 \quad [1]$$

where Ψ is the transform operator in which the reconstructed data, m , is sparse, \mathcal{F}_u is the undersampled Fourier transform, y is the sampled data, ϵ is a fidelity factor, and $\|x\|_n$ is the ℓ_n norm: $\|x\|_n = (\sum_i |x_i|^n)^{1/n}$, for $n > 0$. The minimization of the ℓ_1 -norm in Eq. 1 promotes sparsity by trying to reduce the number of nonzero coefficients as much as possible. The ℓ_1 -norm objective function is offset by the ℓ_2 -norm constraint that the reconstruction remains consistent with the measured data within the tolerance, ϵ .

In MRI, wavelets have been the popular transform domain in which the ℓ_1 -norm is minimized. However, in this work, the data is undersampled in the $k_y t_1$ plane in which the wavelet transform may not necessarily be as optimal as in MRI. As described by Lustig et al., minimizing finite differences ($\Psi = \nabla$), or total variation (TV), can also be used alongside the wavelet transform as a form of smoothing the data (12). Other work has shown that minimizing TV alone is sufficient to adequately reconstruct undersampled datasets (13,21,22). Here, we use TV exclusively to sparsify the data.

The constrained problem in Eq. 1 can alternatively be written as an unconstrained problem

$$\min_m \|\nabla_{y,F_1} m\|_1 + \frac{\lambda}{2} \|\mathcal{F}_u m - y\|_2^2 \quad [2]$$

where λ is a regularization parameter that weighs the sparsity against the data consistency, $m = S(x, y, F_1, F_2)$ is the final dataset, \mathcal{F}_u is applied only along the y and F_1 dimensions, $y = s(x, k_y, t_1, F_2)$ is the sampled data, and ∇_{y,F_1} is the gradient in the yF_1 plane.

In a fully sampled EP-JRESI sequence, the final 4D dataset, $S(x, y, F_1, F_2) = \mathcal{F}\{s(k_x, k_y, t_1, t_2)\}$, is composed of two spatial and two spectral dimensions. The simplest way to visualize the data is to consider that for every point in the xy spatial plane (voxel), there is a 2D J -resolved spectrum (F_1, F_2). An example of this is shown in Fig. 1a,b. Experimentally, the data is collected such that the entire $k_x t_2$ plane is acquired during a single EPSI readout for a given (k_y, t_1) point. Nonuniformly undersampling the $k_y t_1$ plane will result in incoherent aliasing in the yF_1 plane following Fourier transform. Figure 1c shows the yF_1 plane for the choline peak at 3.2 ppm (dotted line in 1B) for a given point along the x -direction (dotted line in 1A). Figure 1c also shows the finite differences along the y and F_1 dimensions. While it can be seen that the yF_1 plane appears sparse within the identity domain ($\Psi = \mathbb{1}$), it can be seen that $\|\nabla m\|_1 < \|\mathbb{1}m\|_1$, as sought out by Eq. 1, and thus minimizing the finite differences are well suited for CS reconstruction. The optimal sparsifying transform for a given application is not yet known and is the subject of ongoing research (23).

METHODS

Phantom

To determine the feasibility as well as evaluate the performance of the CS reconstruction, numerous retrospective undersampling and reconstructions were performed on a fully sampled prostate EP-JRESI phantom dataset. A 500 mL prostate phantom was prepared containing the following metabolites at physiological concentrations as reported in healthy human prostate (24,25): citrate (Cit, 50 mM), creatine (Cr, 5 mM), choline (Cho, 1 mM), spermine (Spm, 6 mM), myo-inositol (mI, 10 mM), phosphocholine (PCh, 2 mM), taurine (Tau, 3 mM), glutamate (Glu, 4 mM), glutamine (Gln, 2.5 mM) and scyllo-inositol (Scy, 0.8 mM). The dataset was localized with a field of view (FOV) of $16 \times 16 \text{ cm}^2$ on a 16×16 grid with a slice thickness of 2 cm for an individual voxel volume of 2 cm^3 ; 512 bipolar gradient echo pairs (t_2 samples) were collected with a repeat time of 0.84 ms and $100t_1$ increments with $\Delta t_1 = 1 \text{ ms}$ resulting in F_1 and F_2 bandwidths of 1000 Hz and 1190 Hz, respectively. With pulse repetition time/echo time = 1500/30 ms and one average, the EP-JRESI phantom scan duration was 40 mins. Water suppression was performed using the WET sequence (26) just before PRESS localization (27). To correct for eddy-currents generated by the EPSI readout, a nonwater-suppressed scan was acquired as a reference (28).

The NUS was simulated by zeroing data points in the fully sampled $k_y t_1$ plane according to the exponentially decaying sampling density

$$\rho(k_y, t_1) = \exp \left\{ -\frac{|k_y|}{a} - \frac{t_1}{b} \right\} \quad [3]$$

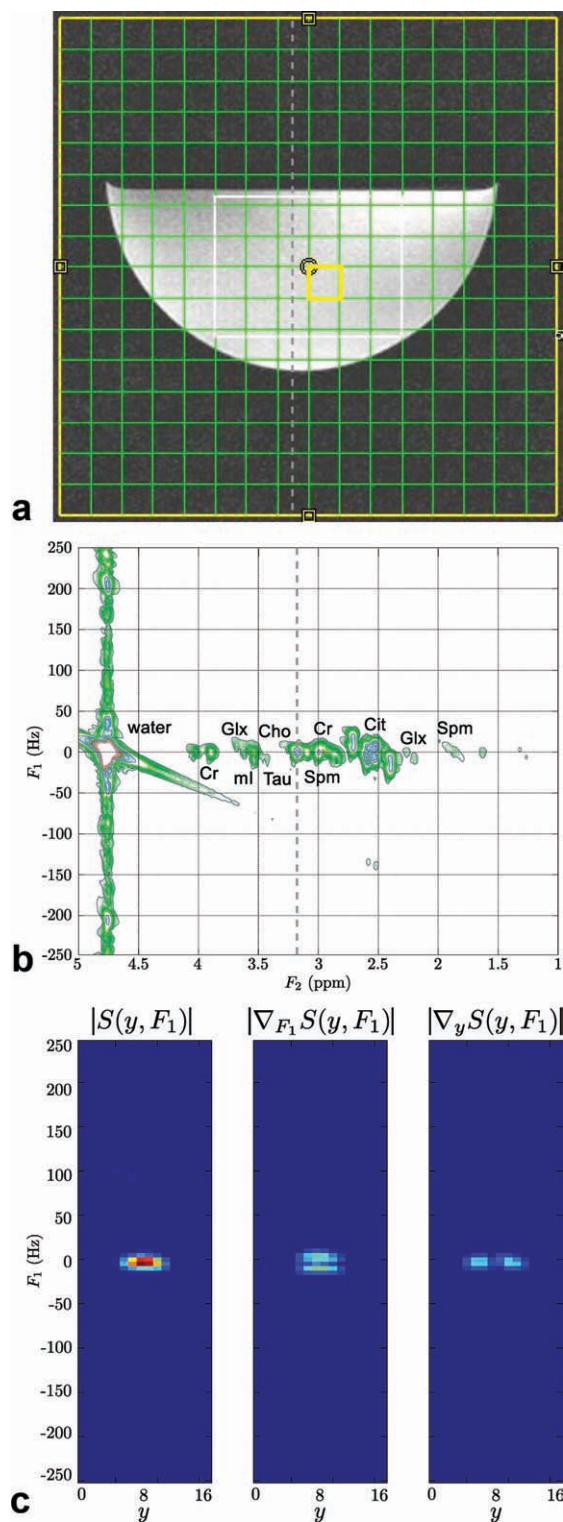


FIG. 1. **a**: T_1 -weighted axial MRI of a prostate phantom where the white box indicates the PRESS localized volume. **b**: 2D J -resolved spectrum from the center voxel (yellow box in **a**) of the prostate phantom. **c**: Demonstration of the sparsity of the undersampled yF_1 plane, $S(y, F_1)$, for a given x and F_2 point as indicated by the dotted lines in **(a)** and **(b)** as well as the finite differences of the same plane, $\nabla_{y,F_1} S(y, F_1)$.

where $\rho(k_y, t_1)$ is the probability a data point is sampled, $-k_{y,\max} \leq k_y \leq k_{y,\max}$, $0 \leq t_1 \leq t_{1,\max}$, and a and b are flexible parameters that determine the percentage of data that is sampled. The signal in the indirect t_1 dimension has an exponential decay envelope determined by T_2 -weighting and the center of k -space has the highest signal intensity. Therefore, Eq. 3 ensures that the regions in the $k_y t_1$ plane with the greatest signal-to-noise ratio (SNR) are collected. Different trials were conducted for NUS, keeping 50%, 33%, 25%, 20%, 16%, and 10% of the original phantom data, corresponding to acceleration factors from 2 to 10 times. For each simulation, a different mask was randomly generated with $a = b$ such that the degree of undersampling was distributed equally between the k_y and t_1 dimensions.

In Vivo

The performance of the reconstruction algorithm was tested in vivo by collecting undersampled data in the prostate of 6 healthy volunteers (age range 25-57 years old) using a body matrix “receive assembly” on a Siemens 3T Trio-TIM MRI scanner (Siemens Medical Solutions, Erlangen, Germany) running the VB17a platform. The FOV was a $16 \times 16 \text{ cm}^2$ area localized onto a 16×16 grid with slice thickness of 2 cm, for an individual voxel volume of 2 cm^3 . The usual fully sampled data consists of 64 t_1 increments. The scanner was programmed to collect only 25% of the fully sampled data matrix according to the sampling density in Eq. 3. Points that were not collected were set to zero. Two averages were acquired for a total scan duration of 12 min 48 s. A nonwater-suppressed scan was also acquired as a reference scan for eddy-current correction and coil combination purposes by fully sampling k_y with only the first t_1 increment, adding 30 s to the total scan duration.

Reconstruction

All data reconstructions were performed by solving Eq. 2 using the split Bregman iterative method (29) with $\lambda = 1$ such that the data fidelity is weighed equally against the minimization of the finite differences. The algorithm was iterated until $\nabla_{y,F_1} m$ was minimized while maintaining a normalized error of no greater than 1 part per million (ppm), namely $\|\mathcal{F}_u m - y\|_2^2 < 1 \times 10^{-6}$. While the reconstruction was performed on the entire dataset, the TV operator, ∇_{y,F_1} , only acted on data in the undersampled $k_y t_1$ plane. The entire 4D reconstruction required roughly 30 mins/channel on a standard desktop PC.

For both phantom and in vivo scans, we have used the maximum-echo sampling method as reported by Schulte et al. (30). This yields a spectrum with a COSY-like diagonal where the J -resolved peaks are centered around the diagonal. Each t_1 row was time-shifted during postprocessing such that the diagonal is rotated 45° , having the appearance of a conventional 2D J -resolved spectrum (31) with an F_1 bandwidth of $\pm 250 \text{ Hz}$.

For the phantom, the CS reconstruction was applied to a processed fully-sampled dataset that had NUS imposed retrospectively. However, for the in vivo scan more steps were required since the raw metabolite data itself was undersampled. A nonwater-suppressed scan was collected to correct for eddy current distortions and to serve as

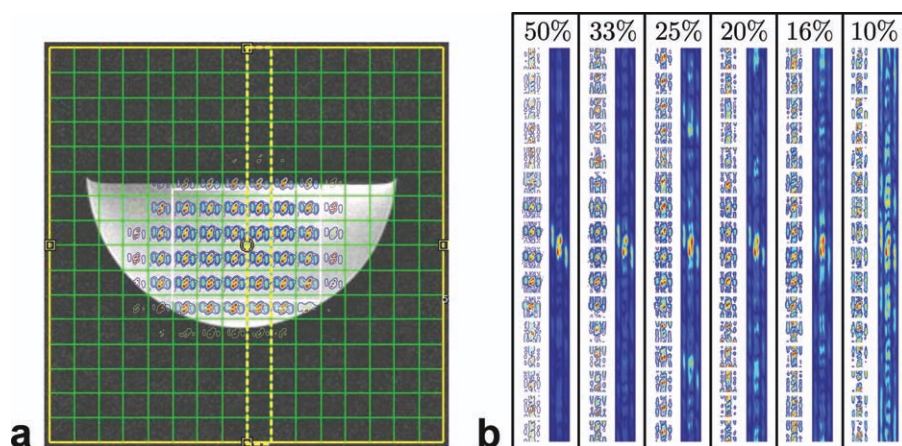


FIG. 2. **a**: Spatial distribution of the fully sampled J -resolved citrate multiplet at 2.6 ppm on the T_1 -weighted axial MRI. **b**: The effect of the incoherent aliasing along both the y -direction as well as the F_1 -dimension as a function of the percentage of the nonuniformly sampled data. For each amount of kept data, the column along the y -direction for a given point along x (left column) is marked by the dotted yellow box in (a), and the F_1 column (right column) is centered around the citrate multiplet at $F_2 = 2.6$ ppm.

a reference for coil combination. The 4D reconstruction was performed on the raw metabolite data for each channel individually, followed by eddy-current correction and coil combination. For a quantitative comparison of the in vivo data, the Creatine+Spermine+Choline to Citrate ratio, $(Cr+Spm+Cho)/Cit$, can be measured by calculating the volume integrals of the diagonal and cross peaks between 2.9 and 3.3 ppm for Cr+Spm+Cho, and between 2.4 and 2.8 ppm for Cit.

RESULTS

Phantom

There are many ways to view the 4D dataset. One simple way is to view each 2D voxel as containing an individual 2D spectra. Although intuitive, it can be cumbersome to view all spectra at once, in the case of a 16×16 imaging grid there are 256 different spectra. For simplicity, a chosen peak can be overlaid on top of a localization image to show the spatial distribution of that peak, as shown with the strongly coupled (AB) citrate multiplet (32,33) (centered at $F_2 = 2.6$ ppm) in Fig. 2a. Although there seems to be some leakage from the point spread function as well as chemical shift artifacts, the peaks with the brightest intensity appear within the PRESS excitation volume marked by the white box.

The effect of NUS leads to incoherent aliasing as shown in Fig. 2b with data that has been filled simply using zeros. To simplify viewing the data, one column (marked by the dotted yellow box in 2a) was selected to display the incoherent aliasing along the y -direction, and one region centered around the citrate multiplet (centered at $F_2 = 2.6$ ppm) is shown to display the incoherent aliasing in the F_1 dimension. For 50% of the data, there is noticeable leakage of the citrate multiplet in the y -direction. The peaks from the fully sampled data shown in 2a are better resolved than the under-sampled peaks in Fig. 2b (first column in each pair) and still maintain the same shape across the PRESS excitation volume. The same can be said along the F_1 dimension where signal leakage is taking place due to the NUS in Fig. 2b (second column in each pair). As the number of sampled points is reduced, the degree of incoherent aliasing along both the y and F_1 dimensions increases. At 16%, most of the original shape has been

heavily degraded as the signal now appears to be incoherently smeared across both y and F_1 dimensions. By 10%, there is little resemblance to the original dataset.

The CS reconstruction of the undersampled phantom datasets along with the normalized root mean square error (RMSE), calculated with respect to the fully sampled data, is shown in Fig. 3. The same column and citrate region in Fig. 2 are displayed in 3a. It can be seen visually and from the low RMSE values that the CS reconstruction successfully cleans up the incoherent aliasing produced by the NUS when Figs. 2 and 3 are compared. For as little as 20% of the original sample points, the spatial reconstruction of the citrate multiplet is very close to the original fully sampled data (yellow box in Fig. 2a). At 16% of the original data, it can be seen that while the spatial distribution along the y -direction is still consistent with the fully sampled data, the shape of the peaks starts to deviate slightly. The same can be seen for the reconstruction of the F_1 dimension where the algorithm performs well in removing the incoherent aliasing. Again, at 16% of the original sample points, there begins to be slight deviations in the shape of the peak (reflected by the notably higher RMSE) when compared to datasets with higher percentages of the original sample points. At 10% of the data, it can be seen that while a lot of the incoherent aliasing has been removed, the final reconstruction has noticeable visual deviations from the original dataset, along with an RMSE above 1%.

Figure 3b is CS reconstructed spectra from only 20% of the original data, taken from the same location as the example spectra in Fig. 1b. While there are slight differences in noise and contour levels, the same basic features present in the fully sampled spectra are clearly visible in the reconstructed spectra. In particular is the faithful reproduction of the citrate multiplet in which the J -resolved peaks are nicely resolved.

In Vivo

Figure 4 shows the results of the CS reconstruction of an undersampled in vivo scan of a 29-year-old healthy prostate. The mask that was used to sample 25% of the $k_y t_1$ plane is shown in Fig. 4. The spatial distribution of the J -resolved citrate multiplet at 2.6 ppm is shown in Fig. 4b. As in the phantom, the peaks are localized within the PRESS excitation volume (white box) with some slight leakage

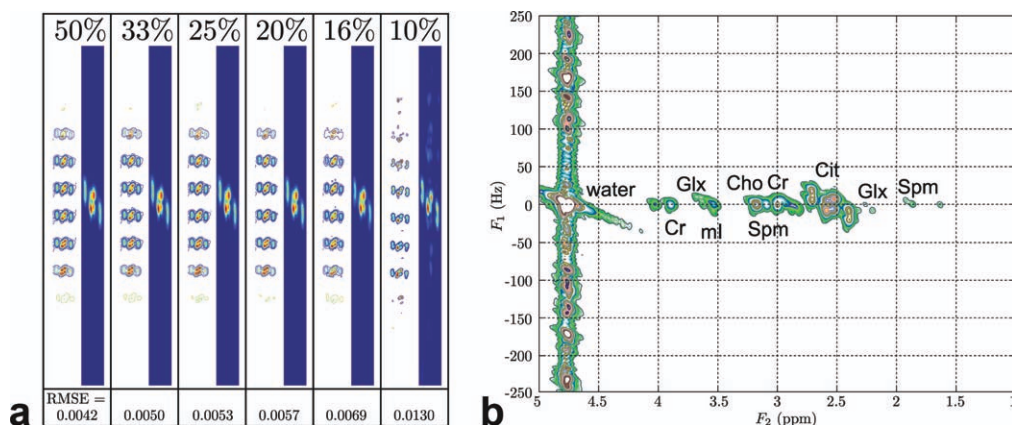


FIG. 3. **a**: Reconstructions of the retrospectively undersampled datasets shown in Fig. 2. The same columns in Fig. 2 are displayed to show the effect of the reconstruction algorithms along with the normalized RMSE values. **b**: A reconstructed spectrum from the same voxel in Fig. 1b with only 20% of the original data from the same voxel as the sample spectrum in Fig. 1b and contains the same annotated metabolites.

due to the point spread function as well as chemical shift artifacts. An individual J -resolved spectrum from a select 2 cm^3 voxel is shown in Fig. 4c. The extracted spectra have considerably more noise than the phantom scans, but the main metabolites, citrate, creatine, spermine, choline, etc. can be detected. For the spectrum shown in Fig. 4b, the $(\text{Cr}+\text{Spm}+\text{Cho})/\text{Cit}$ was calculated to be 0.395. The mean $(\text{Cr}+\text{Spm}+\text{Cho})/\text{Cit}$ value for all six volunteers from a similar location was measured to be 0.451 with a coefficient of variance of 19%, and is consistent with what has been reported in the literature (34,35). To demonstrate the reproducibility between all the scans, the reconstructed citrate multiplet from the left peripheral zone of each volunteer is shown in Fig. 5.

DISCUSSION

The application of CS requires that the fully sampled dataset be sparse in some transform domain and that the NUS pattern be such that any aliasing be incoherent. Since the undersampling performed in the $k_y t_1$ plane of the 4D

EP-JRESI data was shown in Fig. 1c to have a sparse representation using finite differences, it is suitable to use TV minimization in the CS reconstruction. By randomly sampling in the $k_y t_1$ plane according to a probability density (Eq. 3), the data yielded incoherent artifacts that spread across each NUS dimension as seen in Fig. 2b. The incoherent artifacts have the appearance of noisy data and get progressively worse as fewer samples are used in the reconstruction. While the incoherent artifacts are not technically “noise” in the conventional sense in that they are not random, they may be removed by “de-noising” algorithms. Total variation has previously been used as a method for noise removal in images (36) and thus serves as a suitable objective function for the CS reconstruction. The reconstruction can be seen to act as a smoothing algorithm that effectively “de-noises” the data so long as it is consistent with the collected data. Such data-consistent denoising effectively fills in the missing data-points while maintaining the fidelity of the originally sampled data.

As can be seen in Fig. 3, the CS reconstruction successfully cleans up the incoherent artifacts for undersampled

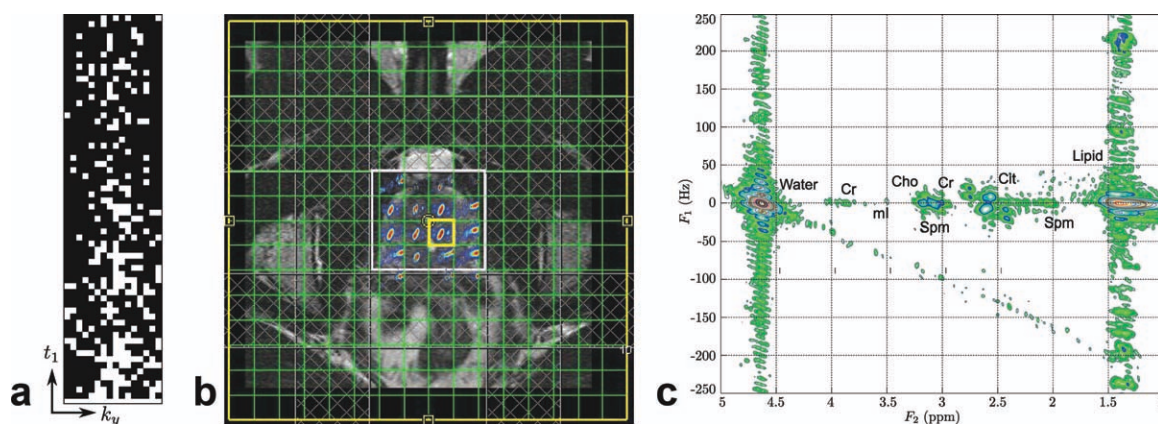


FIG. 4. Reconstruction of an undersampled 4D EP-JRESI in vivo prostate scan with only 25% of the samples as required by the Nyquist-Shannon criterion showing (a) the mask used to undersample the $k_y t_1$ plane where the white points indicate those that were sampled, (b) the multivoxel spatial distribution of the citrate multiplet at 2.6 ppm overlaid on top of the T_2 -weighted axial MRI with the white box indicating the PRESS localization, and (c) a J -resolved spectrum from a select voxel in the reconstruction.

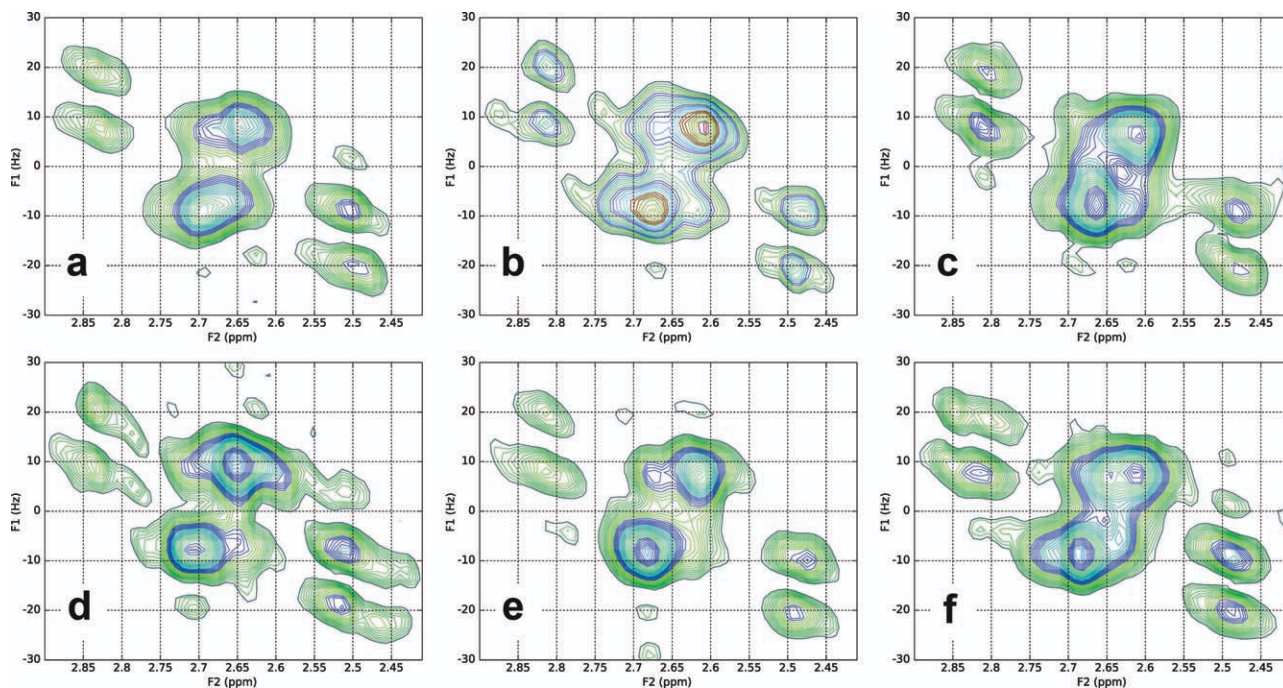


FIG. 5. **a-f**: Expanded view of the citrate multiplet from a select voxel in the left peripheral zone from each of the six healthy male volunteers.

data. For the undersampled data containing more than 20% of the fully sampled data, the reconstruction produces a high fidelity reproduction of the original data, with RMSE values all below 0.6%. The performance of the reconstruction algorithm begins to degrade with fewer sample points, in this case, once the data drops below 20%. Despite the performance drop, it is still remarkable to see that even at 10% of the data, the CS reconstruction does a decent job of cleaning up the incoherent artifacts, with an RMSE of 1.3%, resulting in a yF_1 profile that is similar to the original fully sampled data. This observation can be useful if a high-fidelity reconstruction is not required, and the data can be undersampled to a higher degree to save time. As expected, the RMSE values increase with the acceleration factor demonstrating the tradeoff between acceleration and accuracy of the reconstruction.

The undersampled in vivo results demonstrate the feasibility in reducing scan times in multidimensional spectroscopic imaging sequences by means of nonuniformly sampling the $k_y t_1$ plane and CS reconstruction. While collecting only 25% of the data results in an acceleration factor of 4, two averages were acquired for SNR purposes, thus resulting in only a 2-fold acceleration. Alternatively, collecting 50% of the data with only 1 average would result in the same acceleration factor as well as the same SNR. However, without sufficient SNR, many of the lower concentration metabolites run the risk of being de-noised, or wiped out completely by the reconstruction, as the data fidelity term in the objective function allows for the modification of features on the order of the noise-level. Since the phantom reconstruction with 25% of the data was comparable to the reconstruction with 50% of the data, only 25% of the in vivo data was collected with two averages in an attempt to boost the SNR of the metabolites with lower sensitivity. The minimum SNR for reconstruction, which

depends on the overall sparsity of a particular signal as well as the extent of the incoherent aliasing is an ongoing field of research and will be the subject of future work (37). Given improved sensitivity (such as better shimming, more sensitive coils, and/or higher B_0), the SNR would be sufficient without having to average, yielding a full acceleration factor of 4.

As the 4D in vivo dataset was actually undersampled during the scan, there is no direct means to compare with a fully sampled dataset as was the case with the reconstructions on the phantom dataset. The reconstructed in vivo spectra and profiles recorded in the 6 healthy controls show similar quality to previously reported fully sampled EP-JRESI spectra acquired in the prostate of healthy volunteers (9). The citrate multiplet is well reconstructed showing a nicely J -resolved AB-type structure. The other major metabolites are visible as well, in which their calculated ratios are in agreement with the literature and consistent throughout all the volunteer scans.

This pilot study made use of randomly generated sampling masks according to Eq. 3 to selectively delete points in the fully sampled dataset to simulate undersampling. The same type of randomly generated sampling mask was used on the MRI scanner to collect an undersampled in vivo dataset. While this technique satisfies the incoherent aliasing criterion in CS, it is not necessarily the optimal sampling scheme. Not all sampled points have equal contribution to the overall structure of the data, and it can be seen that the collection of certain points can be more critical than other points. That is not to say that certain points are unimportant, but rather the collection of certain key points can be critical such as the point at $k_y = 0$ and $t_1 = 0$. Likewise, it is possible that for some applications, one of the dimensions in the yF_1 plane may be more sparse than the other, and so the values for a and b (which were

set to be equal in this study) can be adjusted accordingly. This may be an even larger concern for the echo-planar correlated spectroscopic imaging sequence since the cross peak signals have a J -dependent maximum intensity in the t_1 dimension and thus cannot be modeled as simple decaying exponentials like in Eq. 3. As a result, determining the optimal sampling masks for both EP-JRESI as well as echo-planar correlated spectroscopic imaging is the subject of further investigation and will be reported elsewhere.

CONCLUSION

In the acquisition of a 4D spectroscopic imaging sequence (2D spatial, 2D spectral), an EPSI readout can be used to simultaneously accelerate the collection of one spatial and one spectral dimension. This is the first in vivo study to show that CS can be used to simultaneously accelerate the acquisition of the remaining spatial and spectral dimensions. Two techniques have thus been combined, both of which simultaneously accelerate the collection of one spatial and one spectral dimension. Such acceleration has the potential to bring 4D spectroscopic imaging (2D spatial and 2D spectral) scan times well under the coveted 10 min barrier, allowing for the power of 2D in vivo MRS to become a clinical reality.

REFERENCES

- Negendank W. Studies of human tumors by MRS: a Review. *NMR Biomed* 1992;5:303–324.
- Aue W, Bartholdi E, Ernst R. Two-dimensional spectroscopy. Application to nuclear magnetic resonance. *J Chem Phys* 1976;64:2229–2246.
- Ryner L, Sorenson J, Thomas M. Localized 2D J-resolved 1H MR spectroscopy: strong coupling effects in vitro and in vivo. *Magn Reson Imag* 1995;13:853–869.
- Thomas M, Yue K, Binesh N, Davanzo P, Kumar A, Siegel B, Frye M, Curran J, Lufkin R, Martin P, Guze B. Localized two-dimensional shift correlated MR spectroscopy of human brain. *Magn Reson Med* 2001;46:58–67.
- Mansfield P. Spatial mapping of the chemical shift in NMR. *J Phys D Appl Phys* 1983;16:L235–L238.
- Posse S, DeCarli C, Le-Bihan D. 3D echo planar spectroscopic imaging at short echo times in human brain. *Radiology* 1994;192:733–738.
- Mulkern R, Panych L. Echo planar spectroscopic imaging. *Concepts Magn Reson* 2001;13:213–237.
- Lipnick S, Verma G, Ramadan S, Furuyama J, Thomas M. Echo planar correlated spectroscopic imaging: implementation and pilot evaluation in human calf in vivo. *Magn Reson Med* 2010;64:947–956.
- Nagarajan R, Furuyama J, Margolis D, Raman S, Sarma M, Thomas M. Echo Planar Based J resolved and correlated spectroscopic imaging of Human Prostate Using External Coil. In: *Proceedings of the ISMRM, Montreal, Canada, 2011*. p 2801.
- Candés E, Romberg J, Tao T. Robust uncertainty principles: exact signal reconstruction from highly incomplete frequency information. *IEEE Trans Inf Theory* 2006;52:489–509.
- Donoho D. Compressed sensing. *IEEE Trans Inf Theory* 2006;52:1289–1306.
- Lustig M, Donoho D, Pauly J. Sparse MRI: the application of compressed sensing for rapid MR imaging. *Magn Reson Med* 2007;58:1182–1195.
- Block K, Uecker M, Frahm J. Undersampled radial MRI with multiple coils. Iterative image reconstruction using a total variation constraint. *Magn Reson Med* 2007;57:1086–1098.
- Drori I. Fast L1 minimization by iterative thresholding for multidimensional NMR spectroscopy. *J Adv Signal Proc* 2007;1:1–10.
- Gamper U, Boesiger P, Kozerke S. Compressed sensing in dynamic MRI. *Magn Reson Med* 2008;59:365–373.
- Kim Y, Narayanan S, Nayak K. Accelerated three-dimensional upper airway MRI using compressed sensing. *Magn Reson Med* 2009;61:1434–1440.
- Liang D, Liu B, Wang J, Ying L. Accelerating SENSE using compressed sensing. *Magn Reson Med* 2009;62:1574–1584.
- Otazo R, Kim D, Axel L, Sodickson D. Combination of compressed sensing and parallel imaging for highly accelerated first-pass cardiac perfusion MRI. *Magn Reson Med* 2010;64:767–776.
- Hu S, Lustig M, Chen A, Crane J, Kerr A, Kelley D, Hurd R, Kurhanewicz J, Nelson S, Pauly J, Vigneron D. Compressed sensing for resolution enhancement of hyperpolarized 13C flyback 3D-MRSI. *J Magn Reson* 2008;192:258–264.
- Lustig M, Donoho D, Santos J, Pauly J. Compressed sensing MRI. *IEEE Signal Process Magn* 2008;25:72–82.
- Huang F, Chen Y, Yin W, Lin W, Ye X, Guo W, Reykowski A. A rapid and robust numerical algorithm for sensitivity encoding with sparsity constraints: self-feeding sparse SENSE. *Magn Reson Med* 2010;64:1078–1088.
- Chang C, Ji J. Compressed sensing MRI with Multichannel data using multicore processors. *Magn Reson Med* 2010;64:1135–1139.
- Bilgin A, Kim Y, Liu F, Nadar M. Dictionary Design for Compressed Sensing MRI. In: *Proceedings of the ISMRM, Stockholm, Sweden, 2010*. p 4887.
- Lange T, Shulte R, Boesiger P. Quantitative J-resolved prostate spectroscopy using two-dimensional prior-knowledge fitting. *Magn Reson Med* 2008;59:966–972.
- DeFeo E, Cheng L. Characterizing human cancer metabolomics with ex vivo 1H HRMAS MRS. *Technol Cancer Res Treat* 2010;9:381–391.
- Ogg R, Kingsley P, Taylor J. WET, a T1 and B1 insensitive water-suppression method for in Vivo localized 1H NMR spectroscopy. *J Magn Reson B* 1994;104:1–10.
- Bottomley P. Spatial localization in NMR spectroscopy in vivo. *Ann NY Acad Sci* 1987;508:333–348.
- Klose U. In vivo proton spectroscopy in presence of Eddy currents. *Magn Reson Med* 1990;14:26–30.
- Goldstein T, Osher S. The split Bregman method for L1-regularized problems. *SIAM J Imaging Sci* 2009;2:323–343.
- Schulte RF and Boesiger P. ProFit: two-dimensional prior-knowledge fitting of J-resolved spectra. *NMR Biomed* 2006;19:255–263.
- Macura S, Brown L. Improved sensitivity and resolution in two-dimensional homonuclear J-resolved NMR spectroscopy of macromolecules. *J Magn Reson* 1982;53:529–535.
- Wilman A, Allen P. The response of the strongly coupled AB system of citrate to typical 1H MRS localization sequences. *J Magn Reson B* 1995;107:25–33.
- Yue K, Marumoto A, Binesh N, Thomas M. 2D JPRESS of human prostates using an endorectal receiver coil. *Magn Reson Med* 2002;47:1059–1064.
- Mueller-Lisse U, Scherr M. Proton MR spectroscopy of the prostate. *Eur J Radiol* 2007;63:351–360.
- Wang X, Wang B, Gao Z, Liu J, Liu Z, Sun QNZ, Yuan Y. 1H-MRSI of prostate cancer: the relationship between metabolite ratio and tumor proliferation. *Eur J Radiol* 2010;73:345–351.
- Rudin L, Osher S, Fatemi E. Nonlinear total variation based noise removal algorithms. *Phys D* 1992;60:259–268.
- Aeron S, Saligrama V, Zhao M. Information theoretic bounds for compressed sensing. *IEEE Trans Inf Theory* 2010;56:5111–5130.